Strong Light-Matter Interaction and its Consequences on Molecular Photophysics

MANUEL HERTZOG

UNIVERSITY OF GOTHENBURG

Department of Chemistry and Molecular Biology
University of Gothenburg
2020

DOCTORAL THESIS

Submitted for fulfilment of the requirements for the degree of
Doctor of Philosophy in Chemistry

Strong Light-Matter Interaction and its Consequences on Molecular Photophysics

MANUEL HERTZOG

ISBN: 978-91-8009-034-6
ISBN: 978-91-8009-035-3

Department of Chemistry and Molecular Biology
SE-412 96 Göteborg
Sweden

Printed by Stema Specialtryck AB
Borås

Trycksak
3041 0234

Ceux qui vivent sont ceux qui luttent

Victor Hugo, Les châtiments

Abstract

Strong light-matter interaction offers the possibility to modify chemical and physical properties of molecules by modifying their photonic environment, resulting in the creation of hybrid light-matter states, known as polaritons. The field of polaritonic chemistry using microfluidic cavities is in its infancy, and developing methods to increase the coupling strength are necessary to maximise the effects of polaritonic states. Moreover, exploring the effect of strong coupling on photophysical properties is necessary.

This thesis covers the design, characterisation and modeling of strongly coupled systems, with the aim of studying photophysical properties and developing methods to increase the total coupling strength between light and matter. Using FT-IR spectroscopy and numerical modeling, an increase of 50% of the coupling strength is reported by aligning the molecular transition dipole moment inside a cavity. Additionally, another method is introduced using artificial plasmonic molecules which increases the coupling strength of a nitrile absorption band by almost an order of magnitude. Furthermore, this thesis shows that upscaling microfluidic cavities is possible without affecting the coupling strength. Finally, selective manipulation of excited states in the strong coupling regime are demonstrated.

This dissertation is an exploratory study of several aspects of strong light-matter coupling paving the way to a new chemistry, and new approaches in material sciences.

Keywords: Strong coupling, Vibropolariton, Polaritonic chemistry

Acknowledgments

First and foremost, I would like to express my very great appreciation to Dr Karl Börjesson, a talented teacher and passionate scientist, whose altruistic time and care were sometimes all that kept me going during my four years of PhD. I also thank Karl for appreciating my research strengths and patiently encouraging me to improve in my weaker areas. I am proud to say my experience in the Molecular material group was intellectually exciting, and has motivated me to continue in academic research. Many thanks also to my co-supervisor Prof Gunnar Nyman and my examiner Prof Johan Bergenholtz for your advices and guidance.

I would like to express my gratitude to Prof David Lidzey, Prof Donatas Zigmantas, Prof Magnus Jonsson and Prof Marica Ericson for accepting to participate in my thesis jury, and for their constructive comments on this dissertation.

I am also very grateful to all collaborators with whom none of my work would have been possible: Prof Timur Shegai, Prof Per Rudquist, Dr Battulga Munkhbat and Dr Denis Baranov from Chalmers University. Special thank to Prof Thomas Ebbesen and Dr James Hutchison from the ISIS in Strasbourg for letting me discover this wonderful world of scientific research during my Master thesis and collaboration during my PhD. All past and current members of the Laboratoires des Nanostructures I had the chance to work with: Thibault, Anoop, Jino, Atef, Hadi, Éloïse, Xiaolan, Cyriaque, Shaojun, Stefano, Robrecht to name a few.

I would also like to thank all the staff that reduces our burdens in dealing with administrative routines. Thank you Linn, Catarina, Ingrid and everyone else.

To all my group members: Jürgen (always good to have someone zooming at 6400% for corrections), Alex, Clara, Chen, Mao, Yizhou, Martin, Yi and Pedro. You are extraordinary people.

Alex, Alica, Rickard, Pedro, Clara and Suman for all the Friday's beers, as

one would say 'and one for the doctor'.

My past and current officemates, Kati, Chen and Mao. Thank you for all the fun and discussions we had together. Khushbu for the amazing chapati party.

Special thanks to Mariza, a amazing person, artist, dancer, skateboarder oregano/olive oil lover.

To the подтягивания/引体向上/barras team, thank you for my writing breaks.

All the present and former colleagues on the 8th floor which I had the pleasure to interact with. Thank you Emma, Marcus, Ruth, Bothulf, Lena, Mari, Jörgen, David, Peter and everyone who gave me all the energy needed during the past years.

Many thoughts to the people from Strasbourg: Jean-Yves, Oussama, Olivia, Nico, Thomas, Odeleine, François, Ziyad, à lui, à elle, à eux, à tout le monde et bien sûr les délicieuses pizza d'*Il Francese* à Strasbourg.

Last but not least special thanks to the R4, Lamajune and everyone for being here after so many years.

List of Publications

The work presented in this thesis is based on research reported in the following research articles, referred to as **Paper I-IV**. The list includes the contributions by the author to each article.

Paper I:
Voltage-controlled switching of strong light-matter interactions using liquid crystals
Manuel Hertzog, Per Rudquist, James A. Hutchison, Jino George, Thomas W. Ebbesen, Karl Börjesson, *Chem. Eur. J.* **2017**, *23*, 18166–18170. [1]

Performed all the experimental work, including the cavity design and fabrication, cleanroom work, optical characterisation and the theoretical analysis. Wrote the manuscript.

Paper II:
Selective manipulation of electronically excited states through strong light-matter interactions
Kati Stranius, Manuel Hertzog, Karl Börjesson, *Nat. Comm.* **2018**, *9*, 2273. [2]

Developed and performed the transfer matrix simulation, performed the theoretical analysis (dispersion analysis, fittings and Hopfield coefficients), helped to design the experimental setup to measure the temperature dependent phosphorescence rate. Contributed to the writing of the manuscript.

Paper III:
The effect of coupling mode in the vibrational strong coupling regime
Manuel Hertzog, Karl Börjesson, *ChemPhotoChem*, **2020**, *4*, 612–617. [3]

Performed all the work, including the cavity design and fabrication, optical characterisation and theoretical analysis. Wrote the manuscript.

Paper IV:
Enhancing light-matter coupling strength beyond the molecular concentration limit
Manuel Hertzog, Battulga Munkhbat, Denis G. Baranov, Timur O. Shegai, Karl Börjesson, *Submitted to Nano Letters* **2020**.

Performed the optical characterisation, cavity preparation (excluding the deposition of the gold nanorods), contributed to the theoretical analysis and co-wrote the manuscript.

Publications not included in this thesis:

Paper V:
Electronic light-matter strong coupling in nanofluidic Fabry-Pérot cavities
Hadi Bahsoun, Thibault Chervy, Anoop Thomas, Karl Börjesson, Manuel Hertzog, Jino George, Éloïse Devaux, Cyriaque Genet, James A. Hutchison, Thomas W. Ebbesen, *ACS Photonics* **2018**, *5* (1), 225-232. [4]

Paper VI:
Angle-independent polariton emission lifetime shown by perylene hybridized to the vacuum field inside a Fabry-Pérot cavity
Jürgen Mony, Manuel Hertzog, Khushbu Kushwaha, Karl Börjesson, *J. Phys. Chem. C* **2018**, *122* (43), 24917–24923. [5]

Paper VII:
Strong light-matter interactions: A new direction within chemistry
Manuel Hertzog, Mao Wang, Jürgen Mony, Karl Börjesson, *Chem. Soc. Rev.* **2019**, *48*, 937-961. [6]

Paper VIII:
Multiplicity conversion based on intramolecular triplet-to-singlet energy transfer
Alexei Cravcenco, Manuel Hertzog, Chen Ye, Muhammad Naeem Iqbal, Uwe Müller, Lars Eriksson, Karl Börjesson, *Sci. Adv.* **5** (9), eaaw5978. [7]

Contents

CHAPTER 1

Introduction

1. A point is that of which there is no part
2. And a line is a length without breadth
3. And the extremities of a line are points

Euclide, Elements

Light and matter has been a source of curiosity and fascination throughout Human history. While seeing the history of the scientific concepts that give the foundation of modern science, it is interesting to see that light and matter were treated as two different entities. Few centuries before common era, the Greek civilisation proposed that the matter is composed of small indivisible particles, latter called atoms from the Greek word ατομος (i.e. indivisible) by John Dalton in 1804. Greek philosophers developed several theories of the fundamental nature of light, the foundations of optics were developed by Euclide in his famous book *Elements*, which defined the axiomatic approach to geometry [8]. Before the start of the second millennium, the Islamic period expanded the knowledge inherited from the Greek civilisation and contributed to the foundation of modern science. For example, Ibn-Sahl excelled in optics and wrote in 984 *On Burning Mirrors and Lenses* in which he discusses the property of lenses and presented a geometric argument based on the sine law of refraction, later known as Snell's law. Few centuries later, the scientific revolution took place. This period was a series of events that marked modern science exemplified

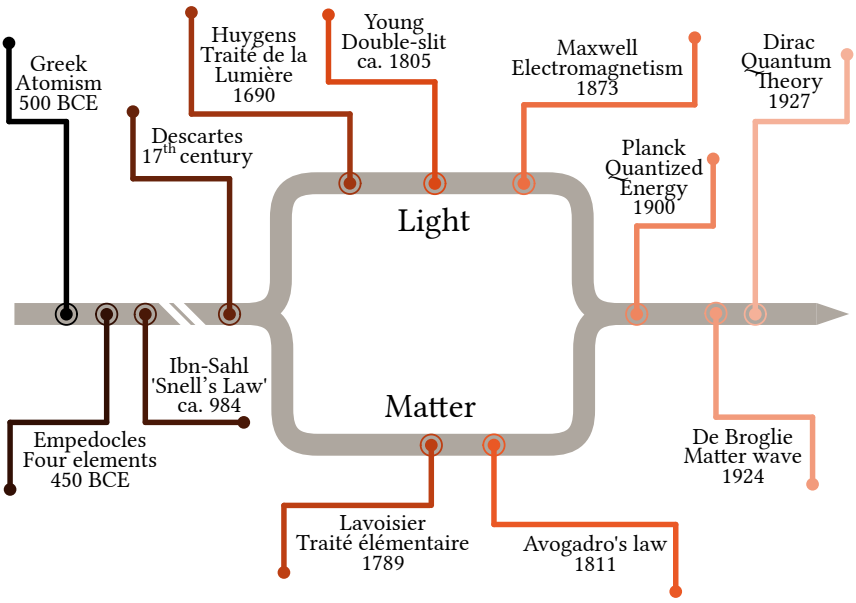

Figure 1.1 Historical timeline of few major discoveries in the history of light-matter interaction.

by great scientist such as Descartes, Fermat, Lavoisier, Maxwell, Avogadro, just to name a few and intriguing discoveries, like the doublle-slit experiment from Young. which gave a glimpse of the . But it was not until the advent of quantum mechanics in the first half of the twentieth century that the quantum theory of light-matter interaction was developed by Dirac [9] (Fig. 1.1). The interaction between light and matter is ubiquitous in modern life and its understanding has lead to many discoveries impacting our society daily such as photovoltaics [10] or photodynamic therapy [11].

The reductionist approach to light-matter interaction does not take account of some experimental observations. This is because the qualitative properties of a macroscopic system are not a simple sum of the isolated consituents' properties, a phenomenon known as emergence and described by Anderson in his seminal paper 'More is different' published in 1972 [12]. Such phenomenon can

be observed in the self-aggregation of organic dyes, known as J-aggregates or H-aggregates. In those systems, the Coulombic interaction between molecules is significant when the intermolecular distance is small. Therefore, a resonant transfer of the excitation energy occurs between molecules resulting in a delocalisation of the excitation [13]. If the coupling is strong [14], the system will be characterised with new eigenstates giving rise to new optical properties as compared to an isolated molecule [15].

In a similar way as exciton coupling, molecules can be affected by its surrounding electromagnetic environment. For example the radiative decay of a molecule close to a metallic surface may be altered [16]. When the coupling to the electromagnetic environment is strong enough, hybrid light-matter states, called polaritons, will emerge. This was first reported by Yakovlev et al. in 1975 [17]. Similarly, Pockrand et al. reported in 1982 strong coupling between Langmuir-Blodgett monolayer assemblies and a surface plasmon [18]. The next 25 years have lead to numerous progress using inorganic materials with the demonstration of polariton Bose-Einstein condensates [19–21], superfluidity [22, 23] or topological polaritons [24] among many others. Even though the considerable amount of literature published based on inorganics and organic material in the weak-coupling regime [25–28], the first experimental observation of strong light-matter interaction using organic molecules was published in 1998 by Lidzey et al. in a pioneering paper [29] and was theoretically introduced the year before by Agranovich et al. [30]. Due to their large transition dipole moment, organic molecules enable to explore the effect of strong-coupling at room temperature. Since the first demonstration of strong coupling with organic molecules, the field has been renewed and enormous amount of effort has been accomplished both experimentally [4, 5, 31–52] and theoretically [53–72].

A phenomenon, which has recently attracted a lot of interest is vibrational strong-coupling. The early reports on vibrational strong-coupling has motivated Ebbesen and coworkers to move the field towards organic chemistry, paving the way to a new field known today as polaritonic chemistry. Driven by experimental progress, an exciting field of applications has emerged at the interface between quantum electrodynamics, chemistry and material sciences.

Exploring the effect of strong coupling on photophysical properties is important in order to unveil the potential of strong light-matter interactions. Furthermore, it is therefore important to develop methods to increase the coupling strength in order to maximise the effect of strong coupling.

In this thesis, general background of light-matter interactions and experimental observations will be presented, as well as the scientific methods used in **Papers I–IV**. The structure of this thesis is as follows: to begin, in chapter 2, the basic concepts of light-matter interactions, in the visible and infrared region, will be introduced. Some general concepts of spectroscopy will be presented to give the reader an introduction to the theoretical background of the experimental techniques used. This chapter also introduces an overview of nematic liquid crystals and localised surface plasmon resonances. Thereafter, chapter 3 deals with the description of strong light-matter coupling, as well as experimental observations. The core concepts of strong-coupling will be discussed to give the reader a fundamental introduction to the topic. In chapter 4, experimental methods on how to fabricate optical cavities as well as the techniques used to quantify their properties are described, since the core of this thesis is based on experimental observations. Finally, in chapter 5, a summary of the main findings will be presented as well as an outlook will be discussed.

CHAPTER 2

Molecular Interactions with an Electromagnetic Field

Oui, il est très tard ; je viens d'éteindre la lampe pour laisser entrer dans ma chambre la lumière de la nuit

Marcelle Sauvageot, Commentaire

In the midst of our daily life, light and matter interact constantly, whether it be photosynthesis or in our eyes. As we take it for granted, understanding the nature of light-matter interaction is fundamental for the research presented in this thesis. This chapter is dedicated to the description of molecules that interact with an electromagnetic field.

2.1 Interactions of light and matter

Electromagnetic (EM) radiation consists of two synchronised oscillating fields, one magnetic **B** and one electric **E**, propagating through space (Fig. 2.1). Electromagnetic waves are classified using their corresponding frequency or wavelength. EM waves with a wavelength from ca. 10 nm to 400 nm defines the ultraviolet (UV) region and if the wavelength is ca. 3 µm to 8 µm it is called mid-infrared (MIR). The visible light lays between 400 and 750 nm. Those are the spectral regions used during my research.

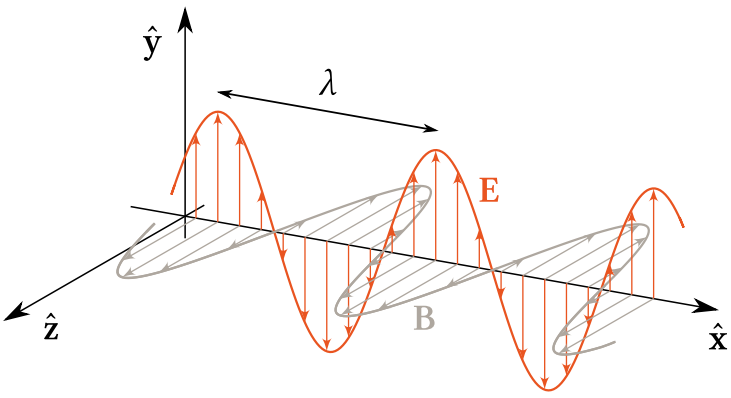

Figure 2.1 An electromagnetic wave propagating in the $\hat{\mathbf{x}}$ direction. The electric field (orange) and magnetic field (grey) oscillate along the $\hat{\mathbf{y}}$ and $\hat{\mathbf{z}}$ directions, respectively. λ defines the spatial period, also called wavelength.

Light can also be seen as discrete packets of energy, referred to as quanta in Einstein's theory of black body radiation [73] and named later as photons by Gilbert Lewis in 1926 [74]. The energy of the photon is related to the frequency through the reduced Planck's constant $\hbar$:

$$E = \hbar\omega\,. \tag{2.1}$$

The most simple interaction between a molecule and light is that one photon is absorbed by one molecule. After absorbing a photon, the molecule is promoted from the electronic ground state to an excited state. A necessary condition to fulfill is that the energy of the incoming light must be equal (or greater) than the energy difference ΔE between the final E_f (excited) and initial E_i (ground) state energies. This condition is the so-called Bohr condition:

$$\hbar\omega = \Delta E = E_f - E_i\,. \tag{2.2}$$

2.1.1 Transition dipole moment

The transitions induced by the electromagnetic field in a molecule are electric-dipole transitions. The oscillating electric field component of the radiation

interacts with electrical charges, i.e. the positive nuclei and negative electrons that constitute an atom or molecule, and cause the transitions observed in absorption and emission spectroscopies. The electric dipole moment $\boldsymbol{\mu}$ operator is defined as:

$$\boldsymbol{\mu} = \sum_{\alpha} q_{\alpha} \mathbf{r}_{\alpha} \,, \tag{2.3}$$

where q_{α} and $\mathbf{r}_{\alpha}$ are the charge and position vector of the α^{th} electron (or nucleus), respectively. The transition dipole moment between an initial state Ψ_i and a final state Ψ_f is:

$$\langle \boldsymbol{\mu} \rangle_{f \leftarrow i} = \langle \Psi_f | \, \hat{\boldsymbol{\mu}} \, | \Psi_i \rangle = \int \Psi_f^* \, \hat{\boldsymbol{\mu}} \, \Psi_i \, \mathrm{d}^3 \mathbf{r} \,. \tag{2.4}$$

The probability $\mathbb{P}$ for a transition to occur is proportional to:

$$\mathbb{P} \propto \left| \int \Psi_f^* \, \hat{\boldsymbol{\mu}} \, \Psi_i \, \mathrm{d}^3 \mathbf{r} \right|^2 \,. \tag{2.5}$$

In order to be able to interact with the electromagnetic field, and therefore absorb (or emit) light, the molecule must possess a dipole oscillating at the same frequency. Only if the transition dipole moment (Eq. 2.4) is non-zero, i.e $\langle \boldsymbol{\mu} \rangle_{f \leftarrow i} \neq 0$, a transition is allowed. Having a closer look at the transition dipole moment leads to specific selection rules, that explain which transitions are allowed in terms of quantum numbers.

2.1.2 Infrared spectroscopy

Let's consider the case of a diatomic molecule in the harmonic oscillator approximation. The vibrational energy levels E_v, resulting from the Schrödinger equation, are given by [75, 76]:

$$E_v = \hbar\omega \left(v + \frac{1}{2} \right) \,, \tag{2.6}$$

where $v = 1, 2, 3 \ldots$ are the vibrational quantum numbers, ω the frequency of the harmonic oscillator with a spring constant k and an effective mass m_{eff} which is expressed as:

$$\omega = \sqrt{\frac{k}{m_{\text{eff}}}} \,. \tag{2.7}$$

The energy of the vibrational states given in terms of wavenumbers are called vibrational terms $\hat{G}(v)$,

$$\tilde{G}(v) = \frac{E_v}{hc} = \frac{1}{2\pi c}\sqrt{\frac{k}{m_{\text{eff}}}}\left(v + \frac{1}{2}\right) = \tilde{\nu}\left(v + \frac{1}{2}\right). \tag{2.8}$$

The gross vibrational selection rule for absorption or emission is that the electric dipole moment of the diatomic molecule must be different when the two atoms are displaced relatively to each others. The transition is said to be infrared active. A permanent dipole moment is therefore not required, only a variation in dipole moment (even from zero). The vibrations that do not induce a change in dipole moment are said to be infrared inactive.

To understand the origin of the gross selection rule, let's have a closer look at the expression of the transition dipole moment defined earlier. Using the definition of the electric dipole moment (Eq. 2.3), the variation in displacement from the equilibrium position (denoted with the subscript 0) can be expressed as a Taylor expansion:

$$\hat{\boldsymbol{\mu}} = \hat{\boldsymbol{\mu}}_0 + \left(\frac{\mathrm{d}\hat{\boldsymbol{\mu}}}{\mathrm{d}x}\right)_0 x + \frac{1}{2!}\left(\frac{\mathrm{d}^2\hat{\boldsymbol{\mu}}}{\mathrm{d}x^2}\right)_0 x^2 + \ldots \tag{2.9}$$

We can rewrite Eq. 2.4 as:

$$\langle \boldsymbol{\mu} \rangle_{f \leftarrow i} = \hat{\boldsymbol{\mu}}_0 \int \Psi^*_{v_f} \Psi_{v_i}\, \mathrm{d}x + \left(\frac{\mathrm{d}\hat{\boldsymbol{\mu}}}{\mathrm{d}x}\right)_0 \int \Psi^*_{v_f} x \Psi_{v_i}\, \mathrm{d}x + \ldots \tag{2.10}$$

The intregral multiplying $\hat{\boldsymbol{\mu}}_0$ is equal to zero[†], hence the transition dipole moment, with $f \neq i$ and keeping only the linear term (first order), is given by:

$$\langle \boldsymbol{\mu} \rangle_{f \leftarrow i} = \left(\frac{\mathrm{d}\hat{\boldsymbol{\mu}}}{\mathrm{d}x}\right)_0 \int \Psi^*_{v_f} x \Psi_{v_i}\, \mathrm{d}x\,. \tag{2.11}$$

It follows that the right-hand side is zero if the dipole moment does not vary with a displacement. To find the specific selection rules for infrared spectroscopy, we have to express the integral of Eq. 2.11 using Hermite polynomials and use

[†] Ψ_{v_f} and Ψ_{v_i} are eigenfunctions of the same Hamiltonian and are orthogonal, which means if $f \neq i \Longrightarrow \langle \Psi_{v_f} | \Psi_{v_i} \rangle = \int \Psi^*_{v_f} \Psi_{v_i}\, \mathrm{d}x = 0$.

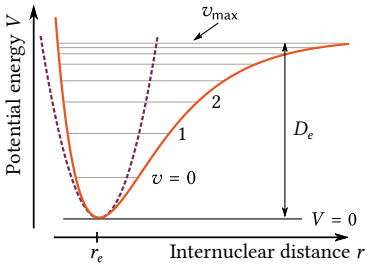

Figure 2.2 The Morse potential (orange) and a harmonic oscillator potential (dashed purple).

their properties [75]. From that, it follows that the transition dipole moment is zero except if $\Delta v = v_f - v_i = \pm 1$. An absorption process corresponds to $\Delta v = +1$ and an emission process to $\Delta v = -1$.

This approach is based on the parabolic approximation of the potential energy of the vibrational terms, i.e. that the vibrational motion obeys Hooke's law. This approximation is reasonable when the displacement r is small relative to the equilibrium position r_e, as shown in Fig. 2.2. Furthermore, this approximation does not take into account the fact that bonds dissociate at an energy D_e where the potential energy curve flattens at $V = D_e$. To take account of this anharmonicity of the potential energy, which is more close to the true potential, Philip M. Morse suggested in 1929 the so-called Morse potential [77]:

$$V(x) = D_e \left[1 - \exp(-ax)\right]^2 , \tag{2.12}$$

where $x = r - r_e$ is the displacement and a is a parameter setting the curvature of the potential and expressed as $a = \sqrt{k/D_e}$. One consequence of anharmonicity is to allow overtones (transitions $2 \longleftarrow 0$, $3 \longleftarrow 0$,...), which are forbidden by the selection rule $\Delta v = \pm 1$, but are weakly allowed compared to the transition $1 \longleftarrow 0$ [78].

For a diatomic molecule, there is only one mode of vibration: the bond stretch. In polyatomic molecules, there are several hundreds of vibrational modes. The vibrational picture of N-atom system is a very complicated motion, a Lissajous motion, which consist of a mixture of bond stretching and angle

bending (examples shown in Table 2.1). Such motions can be decomposed in normal vibrations of the system. The total number of vibrational modes of a N-atom molecule is given by the following rule:

$$\begin{aligned} &\text{Linear molecule:} && 3N - 5 \\ &\text{Nonlinear molecule:} && 3N - 6 \end{aligned}$$

The gross selection rule for infrared spectroscopy applies as well for polyatomic molecules. Consider a harmonic oscillator along x that undergoes a transition $1 \longleftarrow 0$. Hence, the wavefunction Ψ_0 of the ground state is proportional to e^{-x^2} and the wavefunction Ψ_1 of the first excited state is proportional to xe^{-x^2}. Replacing

Table 2.1 Example of fundamental vibration wavenumbers of importance in this thesis. Taken from [79].

Vibration	Compound class	Wavenumbers [cm^{-1}]
O – H stretch	alcohol H-bonded	3550–3200
C – H stretch	aldehyde	2830–2695
C ≡ N stretch	nitrile	2215–2275
C = O stretch	aldehyde	1740–1720
C – H bend	aldehyde	1390–1380

those relations into Eq. 2.4 shows that the excited state wavefunction must have the same symmetry as the displacement x. For specific selection rules, a powerful way of identifying whether transitions are infrared active is to classify them according to their symmetries. Using group theory, each modes can be classified in one of the symmetry species of the molecular point group [75, 80, 81].

2.1.3 Electronic spectroscopy

To understand the electronic selection rules, one must first introduce the concept of electron spin, and the associated quantum numbers.

Electron spin

The spin is an important quantum mechanical property of the electron, i.e. the fact that it possesses an intrinsic angular momentum. To understand the movement of an electron within an atom in a designated orbital, four quantum numbers are used [82]:

1. The principal quantum number $n = 1, 2, \ldots$ which describes the energy level of an electron.

2. The angular quantum number $\ell = 0, 1, 2, \ldots, n-1$ which is related to the magnitude of the angular momentum through $L^2 = \hbar^2 \ell(\ell+1)$.

3. The magnetic quantum number m_ℓ that refers to the projection of the angular momentum in the z-direction. The magnitude L_z of this projection is given by $L_z = m_\ell \hbar$, where $m_\ell = \ell, \ell-1, \ldots, -\ell$.

4. The spin magnetic quantum number m_s, which describes the direction of the electron spin angular momentum s of a particle. For an electron s is $\frac{1}{2}$ and can be oriented in two directions, $m_s = +\frac{1}{2}$ or $m_s = -\frac{1}{2}$, denoted $\uparrow$ or $\downarrow$, respectively.

In an atom, no electrons can have the same four quantum numbers and the lowest energy orbital will be filled first according to the *Aufbauprinzip*, or building-up principle. In brief, for a nucleus of atomic number Z the orbitals are filled in succesion and the order is:

1s 2s 2p 3s 3p 4s 3d 4p ...

where the s orbitals have the quantum number $\ell = 0$, the p orbitals the quantum number $\ell = 1$ and so on. Each orbitals can have two electrons, but they must also obey the Pauli exclusion principle. The Pauli exclusion principle, published in early 1925 [83], states that no more than two electrons can occupy a given orbital, and if they do, then their spins must be paired, i.e. one electron has $m_s = +\frac{1}{2}$, the other has $m_s = -\frac{1}{2}$.

When there is more than one electrons, for example in a typical organic molecule, we must use the total spin angular momentum quantum number S. Consider the case with two electrons with spin s_1 and s_2 (and total spin $S = s_1 + s_2$) and their respective quantum number m_1 and m_2. The corresponding basis states $\left|\frac{1}{2}, m_1\right\rangle \left|\frac{1}{2}, m_2\right\rangle$ are a 4-dimensional space. The total spin and its projection can be obtained by adding the angular momentum using the Clebsch-Gordon coefficients:

$$|S, m\rangle = \sum_{m_1+m_1=m} C^{s_1 s_2 S}_{m_1 m_2 m} |s_1, m_1\rangle |s_2, m_2\rangle \,. \tag{2.13}$$

Substituting in the four basis states $\uparrow\uparrow, \uparrow\downarrow, \downarrow\uparrow$ and $\downarrow\downarrow$ gives the possible values for the total spin. There is one state with a total spin angular momentum S of 0, called the singlet state:

$$|0, 0\rangle = \frac{1}{\sqrt{2}} \left(\uparrow\downarrow - \downarrow\uparrow\right) \,. \tag{2.14}$$

And there are three different states with a total spin angular momentum S of 1, calles triplet states:

$$\begin{aligned} |1, 1\rangle &= \uparrow\uparrow \\ |1, 0\rangle &= \tfrac{1}{\sqrt{2}} \left(\uparrow\downarrow + \downarrow\uparrow\right) \\ |1, -1\rangle &= \downarrow\downarrow \,. \end{aligned} \tag{2.15}$$

Thus, the number of possible orientations describes the spin multiplicity term M [82]:

$$M = 2S + 1 \,. \tag{2.16}$$

In a multi-electron system, higher values of S are permitted, for example if $S = 2$, $M = 5$ there are five different spin orientations and referred to as the quintet state. Furthermore, an additional rule for the building-up principle arises due to the spin multiplicity. This is the so-called Hund's maximum multiplicity rule, which states that for any given configuration, the term of greatest multiplicity is the lowest in energy.

Electronic selection rules

The selection rules for electronic transitions result from an examination of the transition dipole moment, in a similar manner than infrared selection rules. A

photon is a bosonic particle and has an intrinsic spin angular momentum of $s = 1$. In a transition, the total angular momentum must be conserved, the change in angular momentum of the electron must therefore compensate the angular momentum of the photon. The selection rules for an atom are given by:[†]

$$\Delta\ell = \pm 1 \quad \Delta m_\ell = 0, \pm 1\,. \tag{2.17}$$

The principal quantum number n can change independently of ℓ and m_ℓ, allowing $2 \longleftarrow 0$ or $3 \longleftarrow 0$ transitions for example.

To extend the selection rules for the polyatomic case, we must first describe the total angular momentum for complex atoms using the notion of term symbols:

$$^{2S+1}L_J\,, \tag{2.18}$$

where $2S + 1$ is the spin multiplicity term (Eq. 2.16), L the total orbital angular momentum quantum number ($L = \sum_i \ell_i$) and J is the total angular momentum quantum number ($J = S + L$). L is denoted in the same way than the orbital using the *Aufbauprinzip* with uppercase letters: $L = 0 \longrightarrow \mathrm{S}, L = 1 \longrightarrow \mathrm{P}, L = 2 \longrightarrow \mathrm{D}, \ldots$ Therefore, using the same rule of conservation of angular momentum during a transition, the selection rules for many-electrons atoms are:

$$\Delta S = 0 \quad \Delta L = 0, \pm 1 \quad \Delta J = 0, \pm 1 \quad \text{but } J = 0 \nleftrightarrow J = 0\,, \tag{2.19}$$

where $\nleftrightarrow$ denotes a forbidden transition. In addition, the angular momentum of the excited electron must be conserved when interacting with the angular momentum of the photon, i.e. $\Delta\ell = \pm 1$. The selection rules progressively fails when the atomic number Z increases allowing singlet to triplet transitions, where $\Delta S = \pm 1$. This concept can be extended to the term symbols for diatomic molecules [78]:

$$^{2S+1}\Lambda^{(+/-)}_{\Omega,(g/u)}\,, \tag{2.20}$$

[†]The justification lies in the expansion of the transition dipole moment (Eq. 2.4) with $\hat{\boldsymbol{\mu}} = -e\mathbf{r}$ for a given axis in terms of spherical harmonics [75]:

$$\int_0^{2\pi}\int_0^{\pi} Y^*_{\ell_f,m_{\ell,f}}(\theta,\phi)Y_{\ell,m}(\theta,\phi)Y_{\ell_i,m_{\ell,i}}(\theta,\phi)\sin\theta\,\mathrm{d}\theta\,\mathrm{d}\phi\,.$$

The integral is zero unless $\ell_f = \ell_i \pm 1$ and $m_{\ell,f} = m_{\ell,i} + m$.

where Λ and Ω are the projections of the orbital and total angular momentum along the internuclear axis, g/u is the parity (with $g = +1$ and $u = -1$) and $+/-$ is the reflection symmetry along an arbitrary plane containing the internuclear axis. Δ is denoted in the same way than in Eq. 2.19 using Greek uppercase letters: $|\Lambda| = 0 \longrightarrow \Sigma, |\Lambda| = 1 \longrightarrow \Pi, \ldots$ The value of Ω is given by $\Omega = |\Lambda + \Sigma|$, where $\Sigma = \sum_i S_i$. The resulting selection rules, based on the conservation of angular momentum, are:

$$\Delta\Lambda = 0, \pm 1 \quad \Delta S = 0 \quad \Delta\Sigma = 0 \quad \Delta\Omega = 0, \pm 1 \,. \tag{2.21}$$

In addition, there are two rules based on the change in symmetry happening during a transition. The first rule states that only the $\Sigma^+ \leftrightarrow \Sigma^+$ and $\Sigma^- \leftrightarrow \Sigma^-$ transitions are allowed. And the second one states that only transitions that induce a change in parity are allowed. This is known as the Laporte selection rules. Further classifications of electronic states and selection rules of small molecules are based upon symmetry properties [78, 80].

2.1.4 Molecular absorption

At room temperature, the majority of molecules will be in the lowest vibrational level of the ground state and absorption starts therefore from this level. The population of N_j of the j-th vibrational level at a temperature T is given by the Boltzmann distribution [82]:

$$\frac{N_j}{N_0} = \exp\left[-\beta(E_j - E_0)\right] \,, \tag{2.22}$$

where $\beta = (k_B T)^{-1}$. Thus, at room temperature (ca. 293 K), the molecules are in their electronic and vibrational ground states.

The wavelengths at which a molecule absorbs light depends on the energy gap ΔE between the orbitals that are involved in the transition. This energy gap is related to the structure of the molecule. A molecule with only single bonds absorbs light in the UV region, while more complex molecules are associated with the absorption of visible light. Molecular electronic transitions occurring during an excitation are shown in Fig. 2.3. Consequently, an electron is promoted

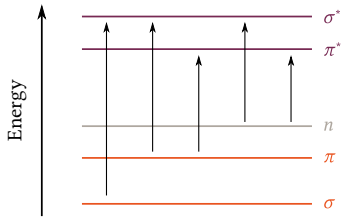

Figure 2.3 Energy levels of electronics transitions.

from an occupied valence orbital (σ, π or n) to an unoccupied antibonding orbital π^* or σ^*. An absorption in a particular spectral region if often due to a particular group of atoms. Like the formation of a π-bond, where two p-orbitals overlap, when more p-orbitals are adjacent, a molecule will form a conjugated π-system. Thus, the energy gap between highest occupied molecular orbital (HOMO) and the lowest unoccupied molecular orbital (LUMO) decreases. In a large organic molecule, these conjugated regions are called chromophores. The longer the conjugated region of the molecule, the lower the energy gap between the HOMO and the LUMO therefore the molecule will absorb lower energy photons. Figure 2.4 shows the molecule β-carotene where eleven carbon-carbon double bonds are conjugated to each other and the $\pi^* \leftarrow \pi$ transition lies in the visible region which explains its characteristic color.

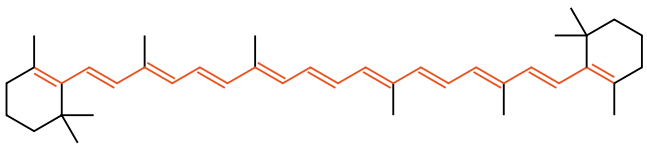

Figure 2.4 Chemical structure of β-carotene. The conjugated carbon-carbon double bonds are highlighted in orange.

2.1.5 The fate of excited states

After initial excitation the molecule is in a higher singlet excited state, denoted as S_n with $n = 1, 2, \ldots$ (the ground state is denoted S_0). A molecule in an

excited state will relax quickly to its vibrationally relaxed state S_1 (or T_1 for the triplet state). Vibrational relaxation is a relaxation process in which the energy is dissipated by interaction with surrounding molecules. It is a thermal decay. Vibrational relaxation is a very fast process (ca. 10^{-12} s). Therefore, all photophysical processes occur from the S_1 (or T_1) state. This is known as the Kasha's rule introduced by Michael Kasha in 1950 [84], which states that the emitting level of a given multiplicity is the lowest excited level of that multiplicity. In this section, non-radiative decay and radiative decay, as well as the concept of spin-orbit coupling, will be briefly presented and are summarised in the Perrin-Jabłoński diagram (Fig. 3.2b).

Spin-orbit coupling

Spin-orbit coupling (SOC) is a relativistic effect that results from the interaction of the spin magnetic moment with the magnetic moment induced by its orbiting in the nuclear electrostatic field. SOC arises in Dirac's theory, which describes the relativistic theory for a $\frac{1}{2}$-spin particle system [85]. Consider a one electron atom, the spin s and the orbital angular momentum ℓ are not separately conserved. They are coupled and the strength of the coupling depends on the relative orientations of the spin and the orbital magnetic moment m, as shown in Fig. 2.5. Therefore, the total angular momentum j, given by $j = \ell + s = \ell \pm \frac{1}{2}$ is high when the two angular momenta are parallel and is low when the two angular momenta are opposed. For treating quantitatively SOC, one must take account of the relative orientation of the spin and the angular momentum is included [86]:

$$\hat{H}_{\mathrm{SO}} = \xi(r)\,\mathbf{l}\cdot\mathbf{s}\,, \tag{2.23}$$

where $\mathbf{l}$ is the orbital angular momentum of the particle moving at a velocity $\mathbf{v}$ ($\mathbf{l} = m_e\mathbf{r}\times\mathbf{v}$) and $\xi(r)$ a function related the electric potential. Therefore, the radial average for the state $|n\ell\, m_\ell\rangle$ of the function ξr yields to the so-called spin-orbit coupling constant $\zeta_{n\ell}$ [86]:

$$\zeta_{n\ell} = \frac{\alpha^2 R_H Z^4}{n^3\ell\left(\ell+\frac{1}{2}\right)(\ell+1)}\,, \tag{2.24}$$

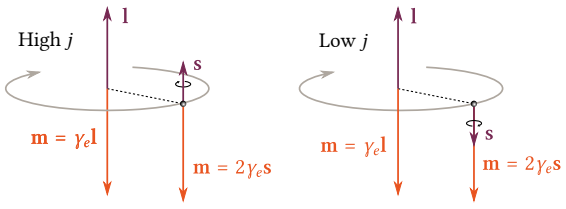

Figure 2.5 Physical picture of spin-orbit coupling. On the left figure the two angular momenta are parallel and antiparallel on the rigth side.

where α is the fine-structure constant, R_H the Rydberg constant and Z the atomic number. Consequently, the strength of the SOC increases sharply when the nuclear charge is high, as $\zeta \propto Z^4$. SOC is also a very important concept for photophysics and photochemistry because it turns spin-forbidden processes, such as intersystem crossing and phosphorescence into allowed transition.

Non-radiative decay

Non-radiative decays of an excited state occurs between two isoenergetic vibrational levels of two different electronic states. Since there is no change in energy, no photon is emitted during the process. Non-radiative decays are irreversible processes because they induce an increase in entropy (higher density of vibrational states in the final excited state) and the subsequent vibrational relaxation occurs very fast (vide supra). Non-radiative transitions between states of equal spin multiplicity are called internal conversion (IC) and those between states of different spin multiplicity are called intersystem crossing (ISC). IC occurring between excited state of same multiplicity, e.g. $S_2 \longrightarrow S_1$ or $T_2 \longrightarrow T_1$ are very fast (ca. 10^{-12} s). The IC from an excited state of any spin multiplicity to the ground state is much slower (ca. 10^{-9} s for $S_0 \longleftarrow S_1$ and ca. 10^{-6} s to seconds for $S_0 \longleftarrow T_0$). ISC crossing involves a change in spin state ($\uparrow\downarrow$ to $\uparrow\uparrow$) and is therefore forbidden in non-relativistic quantum theory. However, ISC crossing is observed when the spin-orbit coupling is significant (Section 2.1.5). Furthermore, the rate of ISC is larger if the transition involves a change in orbital type as described by the El-Sayed's rules [87]. The rate of ISC is also usually increased as the energy

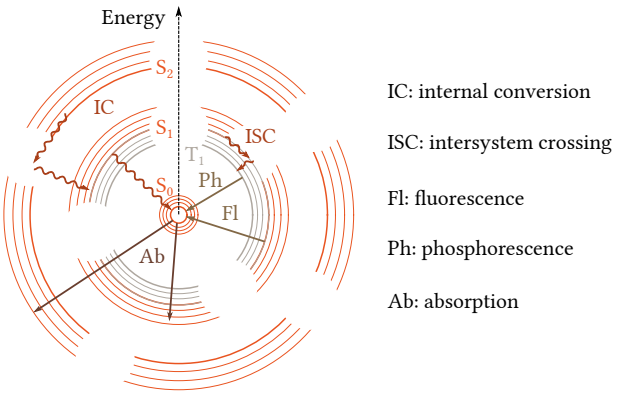

Figure 2.6 Perrin-Jabłoński diagram illustrating the photophysical processes. Straight arrows indicate radiative processes and wavy arrows indicate non-radiative processes.

separation between S_1 and T_1 is smaller [88].

Radiative decay

Radiative decay is a process in which the energy is dissipated by the emission of a photon. There are two main types of radiative decay, fluorescence and phosphorescence. Fluorescence occurs between two states ($S_0 \leftarrow S_1$[†]) of the same spin multiplicity and phosphorescence occurs between the T_1 state and the ground state S_0. Similarly to ISC, phosphorescence is in principle a forbidden transition but can be allowed through spin-orbit coupling.

Rates and quantum yields

The fate of an excited state can be known if the rates of all deactivation processes are known. Let's consider fluorescent molecule X diluted in a solvent whose concentration is $[X]$. After excitation (time $t = 0$ and assuming a short pulse of light) a certain amount of the molecules are in the S_1 state. Then, they can

[†]Some exception exists, for example azulene has $S_0 \leftarrow S_2$ emission.

undergo a transition to the ground state, either radiatively or non-radiatively. The rate of relaxation is given by first order kinetics:

$$-\frac{\mathrm{d}\left[{}^1X^*\right]}{\mathrm{d}t} = (k_r + k_{nr})\left[{}^1X^*\right] , \tag{2.25}$$

where $\left[{}^1X^*\right]$ is the concentration of the excited molecules, k_r and k_{nr} are the rate constants for the radiative and non-radiative processes, respectively. Integration of Eq. 2.25 yields:

$$\left[{}^1X^*\right] = \left[{}^1X^*\right]_0 \exp\left(-\frac{t}{\tau_f}\right) , \tag{2.26}$$

where $\left[{}^1X^*\right]_0$ is the initial concentration of excited molecules and τ_f is the lifetime of the state S_1 given by [89]:

$$\tau_f = \frac{1}{k_r + k_{nr}} . \tag{2.27}$$

If there is more non-radiative decays, the lifetime τ (as well as for phosphorescence) can be generalised as:

$$\tau = \frac{1}{\sum_i k_i} . \tag{2.28}$$

Finally, another important figure of merit can be defined. The emission quantum yield which relates the number of absorbed photons to the number of emitted photons and gives the probability that a molecule undergoes an emissive process. The quantum yield Φ is given by:

$$\Phi = \frac{\text{number of photon emitted}}{\text{number of photon absorbed}} = \frac{k}{\sum_i k_i} . \tag{2.29}$$

2.2 Nematic liquid crystals

The symmetry and mechanical properties of a liquid crystal are intermediate to those of a crystal and those of a liquid. These properties explains the name liquid crystal, which is more formally a mesormophic phase. In the following, we will only consider the case of uniaxial nematic liquid crystals, its name originates from the Greek νήμα (= thread), set out by Georges Friedel and referring to the thread-like defects that are observed in these materials [90]. Most of nematic

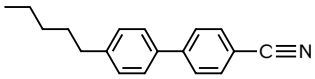

Figure 2.7 Chemical structure of the liquid crystal 5CB. The rigid core is constitued of two phenyl rings with the flexible pentyl group on the left and the carbonitrile permanent dipole on the right.

liquid crystals are calamitic (rod-shaped). The basic building blocks of such molecules are constitued of a rigid core where a terminal permanent dipole is attached at one side and a terminal flexible chain at the other side [91]. A well known example of such a molecule is 4'-pentyl-4-biphenylcarbonitrile (5CB) and was used in this thesis (Fig. 2.7). The rigid core region is constitued of two phenyl rings, within which electrons are delocalised and can respond to an applied external electric field. At one end the pentyl group acts as a flexible chain and at the opposite the carbonitrile acts as a permanent dipole.

One fundamental property of nematic liquid crystal is the orientational order due to the molecular shape anisotropy. In the nematic phase, the center of mass of the molecules have three translational degrees of freedom, making them randomly oriented, hence they do not have a long-range positional order. The order is in the direction of the molecule. Uniaxial nematic liquid crystals have one axis, called directrix, which tends to be align along a particular direction, labeled by a unit vector $\hat{\mathbf{n}}$. The direction of $\hat{\mathbf{n}}$ is arbitrary in space but is usually given by an alignment layer (Section 4.1.4). Figure 2.8 is a snapshot in time of the molecular alignment in three different phases: crystalline, mesomorphic and isotropic. In the crystal, all the molecules are aligned and parallel with the director in opposition with the isotropic phase (liquid) where all the molecules are randomly oriented. In between lies the liquid crystal phase. The nematic order parameter S is used to measure the order of the molecules and defined as [91, 92]:

$$S = \left\langle \frac{3\cos^2\theta - 1}{2} \right\rangle = \frac{1}{2}\int f(\theta)\,(3\cos^2\theta - 1)\,/\,\mathrm{d}\Omega\ , \tag{2.30}$$

where θ is the angle between the molecular long axis and the director $\hat{\mathbf{n}}$, $f(\theta)$ a distribution function giving the probability of finding a rod in a small solid

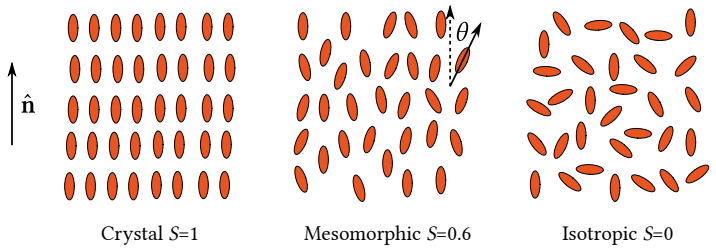

Figure 2.8 Illustration of rod-like liquid crystals exhibiting different amount of orientational order from crystalline to isotropic.

angle $d\Omega$. For example, if $f(\theta)$ is centered around $\theta = 0$ (or π), $\cos\theta = \pm 1$ hence $S = 1$ which is the crystalline phase. At the other hand, if the orientation is random, $\langle \cos^2\theta \rangle = 1/3$[†] and $S = 0$, which is the isotropic phase. Therefore, the order parameter S is a measure of orientation. The order parameter for a liquid crystal is in the interval $S \in [0, 1]$.

2.2.1 Fréedericksz transition

A direct and important consequence of the anisotropic nature of the liquid crystal molecules is the resulting anisotropic physical properties. For instance, the response to an applied electric field will differ according to the dielectric anisotropy of the molecules. The dielectric constants, along $\varepsilon_\parallel$ or perpendicular $\varepsilon_\perp$ to the director $\hat{\mathbf{n}}$, are different and as a consequence the liquid crystals will display a non-zero dielectric anisotropy $\Delta\varepsilon$ [91]:

$$\Delta\varepsilon = \varepsilon_\parallel - \varepsilon_\perp \neq 0\,. \tag{2.31}$$

In practice, to achieve a large positive value of $\Delta\varepsilon$, a strong polar group is attached at one end of the molecule aligned with the long axis, such as the $-\mathrm{C}\equiv\mathrm{N}$ group shown in Fig. 2.7.

When an external electric field is applied, the charges in the rigid core exert a torque which reorient the permanent dipole moment along the direction of

[†]The expectation value of $\cos^2\theta$ over a sphere is given by $\frac{1}{2}\int_0^\pi \cos^2\theta \sin\theta \, d\theta$. Substituting $u = \cos\theta$ and $du = -\sin\theta \, d\theta$ yields to $\frac{1}{3}$.

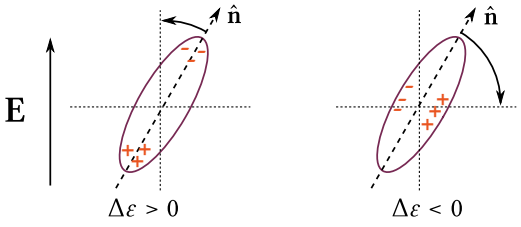

Figure 2.9 Electric field induced reorientation of the director $\hat{\mathbf{n}}$ according to the value of the dielectric anisotropy $\Delta\varepsilon$.

the electric field, the lowest energy configuration. Figure 2.9 illustrates how a nematic liquid crystals will respond to an external electric field. A material with positive dielectric anisotropy, i.e. $\Delta\varepsilon > 0$, will respond to an external electric field by polarizing parallel to the director $\hat{\mathbf{n}}$, in opposition to the case when the dielectric anisotropy is negative, i.e. $\Delta\varepsilon < 0$, the molecule will align perpendicularly to the applied electric field. The influence of the boundary, defined by the alignment layer, opposes the response to the electric field, and yields in a threshold phenomenon called the Fréedericksz transition [93]. Usually, to apply an electric field in a liquid crystal cell, a voltage is applied over the cell (Section 4.1.5). When the voltage V is below the threshold voltage V_T, also called the Fréedericksz voltage, the liquid crystals remain in a homogeneous (planar) alignment as shown in Fig. 2.10. When the voltage applied is above V_T, the directrix of the liquid crystal starts to distort and when $V \gg V_T$, the liquid crystal directrix will align parallel to the applied electric field, also called homeotropic alignment. The director $\hat{\mathbf{n}}$ will still be planar at the boundaries, yielding to a residual planar alignment in the vicinity of the alignment layer (Fig. 2.10).

2.2.2 Optical anisotropy

Another consequence of the anisotropic properties of liquid crystals is the optical anisotropy, also called birefringence. From Fig. 2.9, we can see that the induced dipole moment of the molecule is bigger in the axis parallel or perpendicular to

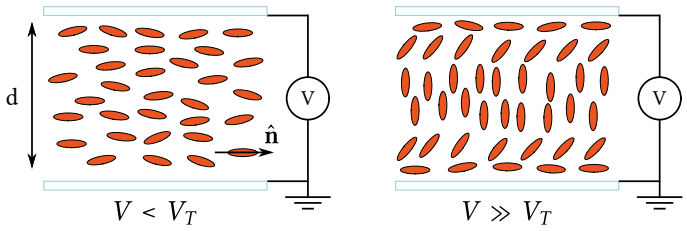

Figure 2.10 Orientation of the directrix inside a cell in response to an applied voltage.

the directrix, hence there is an anisotropy in the polarizability α in the material, i.e. $\alpha_{\parallel} \neq \alpha_{\perp}$. Consequently, an incident polarized light will experience a different refractive index if the molecules are aligned parallel or perpendicularly to the light. Therefore, the material will have two optical axis: one parallel to the director vector $\hat{\mathbf{n}}$ and one perpendicular. The birefringence Δn is defined as the difference between the those two refractive indices:

$$\Delta n = n_{\parallel} - n_{\perp} \neq 0\,. \tag{2.32}$$

Since the electronic polarizability plays a dominant role in the value of the refractive index, for randomly oriented molecules ($S = 0$) the value of Δn would be equal to zero. But for aligned molecules the value of Δn would be, for the alkylcyanobiphenyl molecule used in this thesis, around 0.2 at room temperature [94]. Thus, the birefringence is dependent of the orientation of the molecules and a typical setup shown in Fig. 4.12a, exhibits a voltage (orientation) dependent optical transmission. At zero voltage the homogeneous alignment of the nematic layer acts as a uniform birefringent slab and after the threshold voltage, the birefringence will oscillate between full and half wave plate conditions, hence the optical transmission will oscillate between 0 and 1 as a function of the applied voltage.

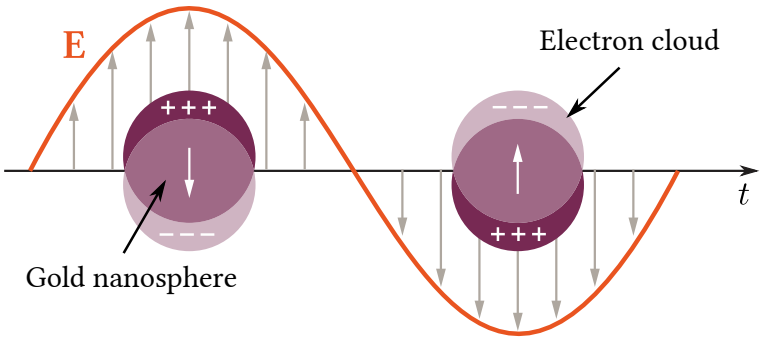

Figure 2.11 Incident light effect on gold nanoparticle inducing an oscillation of the electron cloud.

2.3 Infrared plasmonics

Localised surface plasmons (LSPs) are a combination of two oscillations, the oscillation of the free electron in a metallic nanoparticle, and the oscillation of an incident electromagnetic field. This will cause a coherent oscillation between these two components (Fig. 2.11). When the electron cloud of a nanoparticle is displaced, the cloud starts to oscillate due to a Coulombic attraction between the electrons and the nuclei. The resonance frequency depends on the size, shape, chemical composition and the local dielectric environment surrounding the nanoparticle [95]. This collective oscillation of the electron cloud is called localised surface plasmon resonance. Let's assume a single metallic nanosphere in vacuum. When an incident electromagnetic field hits a nanosphere of radius a, a dipole moment μ is induced and its amplitude is proportional to the strength of the applied field $|\mathbf{E}_0|$. The induced polarizability α, defined as $\boldsymbol{\mu} = \alpha \mathbf{E}_0$, is given, in the quasistatic approximation (the nanosphere is smaller than the incoming wavelength, hence the electric field of the light is assumed to be constant), by [95, 96]:

$$\alpha = 4\pi a^3 \frac{\varepsilon(\omega) - 1}{\varepsilon(\omega) + 2}, \tag{2.33}$$

where $\varepsilon(\omega)$ is the wavelength dependent dielectric constant of the nanosphere. When the denominator of the right-hand side of Eq. 2.33 tends to zero, the

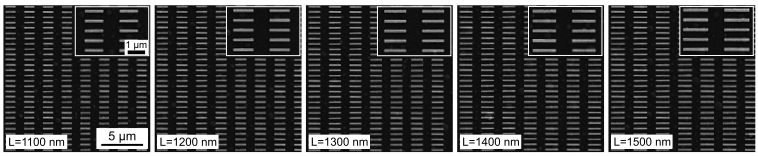

Figure 2.12 Scanning electron microscopy figure of the gold nanorods array used in **Paper IV**.

localised surface plasmon resonance greatly increase the polarizability α. Therefore, the spectral position of the LSP resonances (LSPRs) is found when $\mathrm{Re}[\varepsilon(\omega)] = -2\varepsilon_m$, also known as the Fröhlich condition. One major drawback of LSPRs is their large bandwidth.

2.3.1 Plasmon surface lattice resonances

The dominant contribution to the LSPRs linewidth is the radiative damping. One way to minimise those losses is based on collective resonances induced by a periodic array of metallic nanoparticles (Fig. 2.12), which results to what is known as surface lattice resonances (SLRs) [97, 98]. In a periodic array the electromagnetic field of one nanoparticle may influence the response of the surrounding nanoparticles. This will result in an electromagnetic coupling between individual nanoparticles. The coupling is mediated by a far-field coupling (or Rayleigh anomalies), i.e. the condition where the diffracted waves propagates in the plane of the array. When the size, shape and period of the array are appropriate, the light scattered by the particles into the array will be in phase with the LSPR, hence reinforcing the resonance of the neighbour. Thus, the scattered field will counter the radiative damping of the LSPR and significantly lower the linewidth of the resonance [99–101]. The lattice will thereby enhance the absorption, and the local electric field surrounding the nanoparticles.

CHAPTER 3

The Fate of an Organic Molecule within an Optical Cavity

Les miroirs feraient bien de réfléchir un peu plus avant de renvoyer les images

Jean Cocteau, Le sang d'un poète

In this part of the thesis, we introduce the basic principles of strong light-matter interaction and further extend the concept to experimental observations.

3.1 Strong coupling theory

To understand strong coupling, we can first start with a classical analogy. Let's consider two undamped harmonic oscillators with masses m_1 and m_2 and their respective spring constant k_1 and k_2. The two harmonic oscillators of frequency ω_1 and ω_2 are coupled together with a spring of constant k_c, as shown inFig. 3.1a.

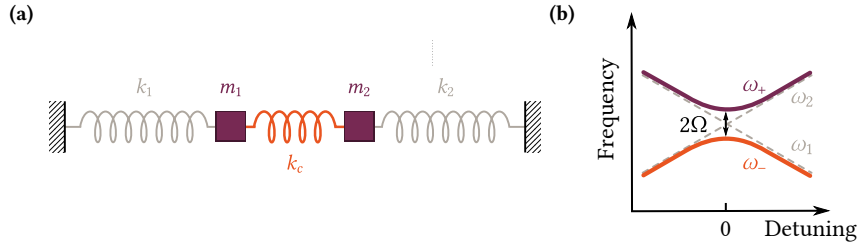

Figure 3.1 (a) Scheme of two harmonic oscillators coupled together. **(b)** Typical anticrossing behaviour resulting from the strong coupling between the two oscillators. The detuning is defined as the difference in frequency between the two coupled oscillators.

Using Newton's second law, the motion of the system can be described by:

$$m_1\ddot{x}_1 + k_1x_1 + k_c(x_1 - x_2) = 0 \tag{3.1a}$$

$$m_2\ddot{x}_2 + k_2x_2 - k_c(x_1 - x_2) = 0\,. \tag{3.1b}$$

After solving Eq. 3.1, two new normal modes of frequency $\omega_\pm$ of the system are obtained:

$$\omega_\pm = \frac{1}{2}\left(\omega_1 + \omega_2 \pm \sqrt{(\omega_1 - \omega_2)^2 + 4\Omega^2}\right)\,, \tag{3.2}$$

where Ω is the splitted frequency. When the system is at resonance, i.e. $\omega_1 = \omega_2 \equiv \omega$, Eq. 3.2 yields to $\omega_\pm = \omega \pm \Omega$. Figure 3.1b shows the two new modes resulting of the strong coupling between the two oscillators and the energy separation between those two modes is known as normal mode splitting. This phenomenon has been observed in macroscopic systems such as coupled springs [102] or acoustic waves [103].

3.1.1 Quantum description of the strong-coupling regime

Vacuum fluctuations are described as the ground state of the electromagnetic field. Their existence is due to the commutation relation $[\hat{x}, \hat{p}] = i\hbar$, which avoids simultaneous vanishing of the kinetic and potential energy. The energy of the ground-state is a compromise between those two energies according to the

Heisenberg's uncertainty relation [75]. This concept was recently directly observed [104] although having been predicted in the beginning of the last century by the pioneering works from Planck [105], Einstein [106] and Nernst[107]. This is a pure quantum effect arising from the quantification of the electromagnetic field. This quantum effect is known to explain the well-known Casimir effect for example [108].

Let's assume an electric field $\mathbf{E}_c$ inside a cavity of frequency ω_r at a point $\mathbf{r}$. In the Heisenberg picture, which provides a link between the classic and quantum picture, it can be written as [109]:

$$\mathbf{E}_c(\mathbf{r}, t) = i\mathcal{E}_0 \left[\boldsymbol{\epsilon}_c f(\mathbf{r}) \hat{a} e^{-i\omega_c t} - \text{h.c.}\right] , \tag{3.3}$$

where $\mathcal{E}_0$ is a normalization factor, $\boldsymbol{\epsilon}_c$ a unit vector representing the field polarisation, $\hat{a}$ the field creation operator, $f(\mathbf{r})$ a function that describes the spatial structure of the field and +h.c. the Hermitian conjugate. The electromagnetic energy of a state of n photons is given by $\hbar\omega_c(n + \frac{1}{2})$, which implies:

$$\langle n| \int \varepsilon_0 |\mathbf{E}_c|^2 \, \mathrm{d}^3\mathbf{r} |n\rangle = \hbar\omega_c \left(n + \frac{1}{2}\right) . \tag{3.4}$$

From that we can extract the field normalisation factor:

$$\mathcal{E}_0 = \sqrt{\frac{\hbar\omega_c}{2\varepsilon_0 \mathcal{V}}} . \tag{3.5}$$

The value of $\mathcal{E}_0$ represent the root mean square of the vacuum electric field amplitude inside a cavity and $\mathcal{V}$ the effective mode volume.

The coupling between a dipole moment $\boldsymbol{\mu}$ (Eq. 2.4) and an electric field $\boldsymbol{\mathcal{E}}$ is expressed as a dipolar coupling. Thus, the coupling V is expressed as:

$$V = \boldsymbol{\mu} \cdot \boldsymbol{\mathcal{E}} . \tag{3.6}$$

To describe the interaction between a molecule, here considered as a two-level system, and the electromagnetic field inside a cavity, the Jaynes-Cummings Hamiltonian (JC) can be used [110]. The Jaynes-Cummings Hamiltonian, within the rotating frame approximation (RWA), is defined as:

$$\begin{aligned} \hat{H} &= \hat{H}_{\text{mol}} + \hat{H}_{\text{cav}} + \hat{H}_{\text{int}} \\ &= \frac{1}{2}\hbar\omega\hat{\sigma}_z + \hbar\omega_c \left(\hat{a}^\dagger \hat{a} + \frac{1}{2}\right) + \hbar g_0 \left(\hat{a}^\dagger \hat{\sigma}_- + \hat{a}\hat{\sigma}_+\right) , \end{aligned} \tag{3.7}$$

where ω and ω_c are the transition frequencies of the molecule and the cavity, respectively, g_0 is the magnitude of the coupling between the cavity and the molecule, $\hat{a}$ and $\hat{a}^\dagger$ are the field creation and annihilation operators, respectively, $\hat{\sigma}_z$, $\hat{\sigma}_-$ and $\hat{\sigma}_+$ are the inversion, raising and lowering operators, respectively, which can be defined using Pauli matrices [75]:[†]

$$\hat{\sigma}_+ = \begin{pmatrix} 0 & 1 \\ 0 & 0 \end{pmatrix} \quad \hat{\sigma}_- = \begin{pmatrix} 0 & 0 \\ 1 & 0 \end{pmatrix} \quad \hat{\sigma}_z = \begin{pmatrix} 1 & 0 \\ 0 & -1 \end{pmatrix}. \tag{3.8}$$

From the interaction term in Eq. 3.7, the underlying mechanism of strong coupling is seen. The term $\hat{a}^\dagger \hat{\sigma}_-$ represents a simultaneous transition between the molecular ground state and its corresponding excited state and the annihilation of a cavity photon (and the reverse process given by $\hat{a}\hat{\sigma}_+$). Thus, highlighting the coherent exchange of energy between the cavity and the molecule.

To extend the JC Hamiltonian to N molecules, which is more relevant in the studies presented in this thesis, the Dicke model can be used, which describes a system of N atoms interacting with a single electromagnetic mode [111]:

$$\hat{H} = \frac{1}{2}\hbar\omega\hat{S}_z + \hbar\omega_c\hat{a}^\dagger\hat{a} + \hbar g_0\left(\hat{a}^\dagger\hat{S}_- + \text{h.c.}\right), \tag{3.9}$$

where the Dicke's collective operators for two-level system $\hat{S}_z = \sum_i^N \sigma_z^{(i)}$ and $\hat{S}_- = \sum_i^N \sigma_-^{(i)}$ have been introduced [112]. Taking the limit where N is large (typically Avogadro number) and a single photon[‡], Eq. 3.9 can be expressed using a Holstein Primakoff transformation, where the Dicke's operators are expressed in terms of bosonic operator $\hat{b}$ [114]:

$$\hat{S}_+ = \hat{b}^\dagger\left(N - \hat{b}^\dagger\hat{b}\right)^{\frac{1}{2}} \quad \hat{S}_- = \left(N - \hat{b}^\dagger\hat{b}\right)^{\frac{1}{2}}\hat{b} \quad \hat{S}_z = \hat{b}^\dagger\hat{b} - \frac{N}{2}. \tag{3.10}$$

Therefore, the Hamiltonian becomes:

$$\hat{H} \simeq \hbar\omega\left(-\frac{N}{2} + \hat{b}^\dagger\hat{b}\right) + \hbar\omega_c\hat{a}^\dagger\hat{a} + \hbar g\left(\hat{a}^\dagger\hat{b} + \text{h.c.}\right), \tag{3.11}$$

[†]Here $\hat{\sigma}_\pm$ are given by $\hat{\sigma}_+ = \frac{1}{2}(\sigma_x + i\sigma_y)$ and $\sigma_- = \frac{1}{2}(\sigma_x - i\sigma_y)$, with σ_x and σ_y are Pauli matrices

[‡]For a typical IR cavity of few microns thick, there is a photon density of ca. 10^6 cm^{-2} and a molecular density of ca. 10^{18} cm^{-2}. Thus a single EM mode is coupled to many molecules [113].

where $g = g_0\sqrt{N}$ is the collective coupling constant. This means that the coupling strength is enhanced by a factor $\sqrt{N}$, which is of fundamental importance meaning that the concentration of molecules coupled to a Fabry-Pérot cavity is the main contributor to the overall coupling strength. One additional resulting property is that the N molecules will behave as a giant quantum oscillator [115].

The Dicke model, which is also known as the Tavis-Cummings Hamiltonian can be diagonalised using the Hopfield-Bogoliubov method [116]. Diagonalisation leads to the eigenstates of the system (dressed states), describing the hybrid light-matter states, known as polaritonic states:

$$\begin{aligned} |\mathrm{P}^+\rangle &= \alpha\,|e,0\rangle + \beta\,|g,1\rangle \\ |\mathrm{P}^-\rangle &= \beta\,|e,0\rangle + \alpha\,|g,1\rangle\ . \end{aligned} \tag{3.12}$$

Thus, the upper ($|\mathrm{P}^+\rangle$) and lower ($|\mathrm{P}^-\rangle$) polaritons are a linear combination of the molecule in the ground state $|g\rangle$ with one photon (denoted with the Fock state $|1\rangle$) and the molecule in the excited state $|e\rangle$ with the absence of photons in the cavity ($|0\rangle$). The composition of the polaritons, i.e. the ratio between the optical and material contribution, are described by the Hopfield coefficients $|\alpha|^2$ and $|\beta|^2$, as shown in Fig. 3.2a. At resonance, the polaritons are hybrid states half matter-half light. The energy separation at resonance between the upper and lower polariton (Fig. 3.2b) defines the so-called Rabi splitting $\hbar\Omega_\mathrm{R}$:

$$\hbar\Omega_\mathrm{R} = 2\hbar g = 2\mu\sqrt{\frac{\hbar\omega_c}{2\varepsilon_0\mathcal{V}}}\boldsymbol{\epsilon}^*\cdot\boldsymbol{\epsilon}_c\,. \tag{3.13}$$

An important property of the hybrid states is their dispersive behaviour resulting from their photonic contribution. Within an optical cavity, the photon modes have a strong in-plane dispersion. Thus the cavity energy can be expressed as [117]:

$$E_c(k_\parallel) = \frac{\hbar c}{n_c}\sqrt{\left(\frac{m\pi}{L_c}\right)^2 + k_\parallel^2}\,, \tag{3.14}$$

where c is the speed of light, n_c the background refractive index, L_c the physical thickness of the cavity and m the cavity mode number. The in-plane wavevector

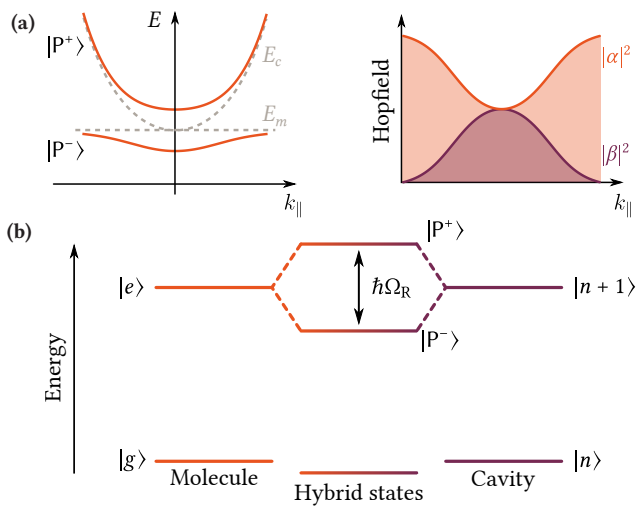

Figure 3.2 (a) Dispersion plot of the polaritonic states at resonance (orange), the cavity dispersion E_c and the molecular absorption E_m are described in the dashed grey lines. The corresponding Hopfield coefficients are displayed on the left figure. **(b)** Perrin-Jabłoński diagram of a coupled molecule-cavity system. The newly formed hybrid states are displayed with the Rabi splitting $\hbar\Omega_R$.

$k_\parallel$ is related to the wavelength of light λ and the angle of incidence θ:

$$k_\parallel = \frac{2\pi}{\lambda} \sin\theta\,. \tag{3.15}$$

The dispersion of the cavity is shown in the left panel of Fig. 3.2a.

3.1.2 Coupled harmonic oscillators

A semi-classical approach can also be used to describe and extract useful information about the system under study. This is done by considering the molecule and the cavity as two coupled harmonic oscillators (CHO), in the same way as previously discussed in the beginning of the chapter. The system can be

described by a 2 × 2 matrix:

$$\begin{pmatrix} E_c - i\hbar\gamma_c & V_a \\ V_a & E_m - i\hbar\gamma_m \end{pmatrix} \begin{pmatrix} \alpha \\ \beta \end{pmatrix} = E \begin{pmatrix} \alpha \\ \beta \end{pmatrix}, \tag{3.16}$$

where E_c and E_m are the cavity and molecule energy with their respective damping constants γ_c and γ_m, and V_a the coupling constant. The CHO model can be solved analytically, and the diagonalisation leads to the eingenvalues, the energy of the upper and lower polaritons:

$$E^{\pm} = \frac{E_c + E_m - i\hbar(\gamma_c + \gamma_m)}{2} \pm \sqrt{V_a^2 + \frac{1}{4}\left(E_m - E_c + i\hbar(\gamma_c - \gamma_m)\right)^2}, \tag{3.17}$$

where the coupling constant V_a is related to the Rabi splitting through:

$$V_a = \frac{1}{2}\sqrt{(\hbar\Omega_{\mathrm{R}})^2 + (\hbar\gamma_c - \hbar\gamma_m)^2}. \tag{3.18}$$

And the following Hopfield coefficients are given by:

$$|\alpha|^2 = \frac{1}{2}\left(1 + \frac{\delta E}{\sqrt{\delta E + 4V_a^2}}\right) \tag{3.19a}$$

$$|\beta|^2 = \frac{1}{2}\left(1 - \frac{\delta E}{\sqrt{\delta E + 4V_a^2}}\right), \tag{3.19b}$$

where $\delta E = E_c - E_m$ is the detuning. The Rabi splitting is defined at resonance, i.e. when $\delta E = 0$, where the energy gap between the upper and the lower polariton is minimum. Therefore, the material and photonic components contribute equally to the newly formed hybrid states and are isoenergetic. The CHO model can be extended to more molecular absorption bands (or cavity modes) by extending the matrix in the left-hand side of Eq. 3.16 to an $N \times N$ matrix.

3.1.3 Dissipation from the system

To define whether a system is in the strong coupling regime, the dissipation processes have to be taken into account. There are three main parameters to look at: the rate κ at which a photon escapes the cavity, the non-radiative decay

rate γ of the molecule, and the coupling strength g. In the time domain, they will define the dynamics of the system. The Rabi frequency Ω_R has to be higher than the dissipation processes of the system, i.e. bandwidth of the molecular absorption $\Delta\omega_m$ and the cavity mode $\Delta\omega_c$. Thus, the system is in the strong coupling regime when:

$$\Omega_R > \frac{1}{2}(\Delta\omega_c + \Delta\omega_m)\,. \tag{3.20}$$

This means that the interaction between light and matter is so strong that the molecules coherently emit and reabsorb the cavity photon, therefore oscillating between its ground and excited states several times before the photon is lost. This is known as the Rabi oscillation.

Another way to quantify the dissipation of the Fabry-Pérot (FP) cavity is the so-called quality factor Q, which is formally defined as the ratio of the energy stored inside the FP cavity and the energy dissipated per cycle:

$$Q \triangleq 2\pi\nu_0 \frac{\text{energy stored}}{\text{energy dissipated}}\,, \tag{3.21}$$

where ν_0 is the resonant frequency expressed in wavenumbers (as used in **Paper III**). Experimentally, the Q-factor is measured as the ratio between the frequency of the FP mode and its corresponding FWHM.

To relate the definition of the Q-factor with common experimental parameters, such as cavity thickness or reflectivity of the mirror inside a FP cavity, we can derived an expression of Q taking account those parameters. To do so, let's start from the definition of the initial stored energy U_0 inside a FP cavity of thickness d. After a short time $\mathrm{d}t$ the energy is reduced to $U(t)$, because light can escape the cavity through the mirrors. Thus, $U(t)$ can be written as:

$$-\,\mathrm{d}U(t) = U(t)\left(\frac{cT}{d}\right)\mathrm{d}t\,, \tag{3.22}$$

which results in:

$$U(t) = U_0 \exp\left(-\frac{cT}{d}t\right) = U_0 \exp\left(-\frac{t}{\tau}\right)\,, \tag{3.23}$$

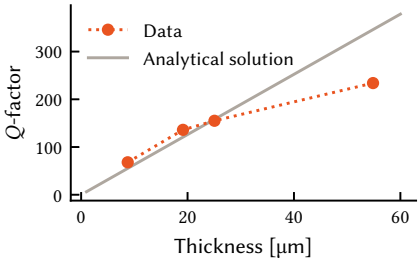

Figure 3.3 Q-factor as a function of the cavity thickness d. The grey line is the expression of Q from Eq. 3.25 and the orange dots are measured data from **Paper III**.

where, c is the speed of light inside the cavity ($c = \frac{c_0}{n}$) and T is the transmittance of the mirrors. The energy dissipation can thus be written as:

$$-\frac{\mathrm{d}U}{\mathrm{d}t} = \frac{cT}{d} U_0 \exp\left(-\frac{cT}{d}t\right) . \tag{3.24}$$

Injecting those two expressions into Eq. 3.21 yields to (assuming no diffractional effects, thus losses are due to reflections (or transmission), thus $T = 1 - r^2$):

$$Q = \frac{2\pi\nu_0 d}{cT} = \frac{2\pi nd}{\lambda_0 T} = \frac{2\pi nd}{\lambda_0(1-r^2)} . \tag{3.25}$$

Figure 3.3 shows the resulting plot of the expression of Q using experimental parameters, which is in good agreement with the measured data.

An additional figure of merit is the ratio η between the coupling strength and the cavity energy. This ratio represents the relative strength of the coupling. If the ratio is greater than 0.10, the system is in the so-called ultra-strong coupling regime (USC) [118]. USC has been observed for organic molecules in the visible regime [119–121] as well as in the infrared [122]. Furthermore, when $\eta > 1$, the system is said to be in the deep strong coupling regime and have been recently shown for the first time in the visible regime using a three-dimensional crystals of plasmonic nanoparticles [123], where they report a coupling ratio of 1.83.

3.2 Transition dipole moment orientation influence on the coupling strength

As seen previously in this chapter (Eq. 3.6), strong light-matter interaction occurs between the transition dipole moment of the molecule and the electric field. Therefore, the coupling strength $\hbar\Omega_R$ is proportional to the dipolar coupling and depends on the relative angle θ between the molecular transition dipole moment $\boldsymbol{\mu}$ and the electric field amplitude $\mathbf{E}_0$:

$$\hbar\Omega_R \propto 2\boldsymbol{\mu}\cdot\mathbf{E}_0 = 2\|\mu\|\|E_0\|\times\cos\theta\,. \tag{3.26}$$

Paper I investigates the influence of the relative angle between the transition dipole moment and the electric field amplitude, a Fabry-Pérot cavity containing the liquid crystal 5CB, was built in order to control the orientation of the molecules (Methods in Sections 4.1.4 and 4.1.5). Figure 3.4a shows the angular dependence between the transition dipole moment of the nitrile group (C≡N) from the liquid crystal 5CB, which is directed in the long axis of the molecule [94], and the incoming electrif field. From the transmission spectra of the empty Fabry-Pérot cavity (Fig. 3.4b), the full width at half maximum (FWHM) is 22 cm^{-1}, yielding to a quality factor of 112. Moreover, Fig. 3.4b shows also the ATR spectrum of 5CB and the corresponding C≡N stretch vibration band centered around 2225 cm^{-1} (FWHM = 10 cm^{-1}). At resonance, the value of the Rabi-splitting is 57 cm^{-1} and 32 cm^{-1} when probing the cavity with polarised light parallel or perpendicular to the director $\hat{\mathbf{n}}$ of the molecule, respectively (Figs. 3.5a to 3.5c). For the two cases, the value of $\hbar\Omega_R$ is greater than the linewidths of both the molecular absorption band and the cavity mode, thus respecting the condition for entering the strong-coupling regime (Eq. 3.20).

Turning now to the experimental evidence of the angular dependence of the coupling strength, Fig. 3.5a shows the transmission spectra of a liquid crystal cell before and after the Fréedericksz transition (Section 2.2.1). When the Fabry-Pérot cavity is probed using in-plane polarised light parallel to the director $\hat{\mathbf{n}}$, the value of $\hbar\Omega_R$ decreases from 57 cm^{-1} to 37 cm^{-1}, as shown in Fig. 3.5a. For the case when the incoming light is polarised perpendicular to the director $\hat{\mathbf{n}}$, the

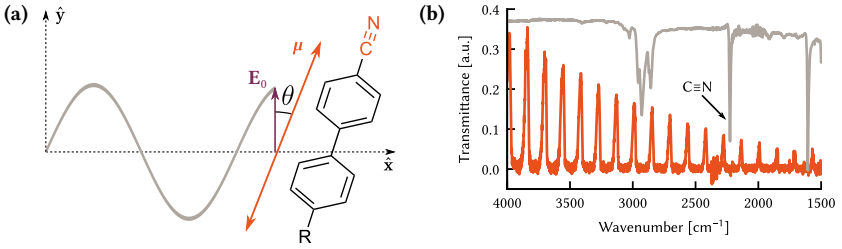

Figure 3.4 (a) Schematic figure showing the angular dependence between the incoming light $\mathbf{E}_0$ and the transition dipole moment $\hat{\boldsymbol{\mu}}$ of the liquid crystal 5CB, molecular structure is shown (R=pentyl). **(b)** Transmission spectra of an empty FP cavity (orange) and ATR spectra of 5CB (grey). The C≡N absorption band coupled to the cavity is shown around 2225 cm^{-1}.

value of the coupling strength remains unchanged (32 cm^{-1}) since the transition dipole moment of the molecule is always perpendicular to the light before and after the Fréedericksz transition (Fig. 3.5b). The difference in the value of $\hbar\Omega_R$ in the two cases is explained by the fact that there is a residual planar alignment in the vicinity of the alignment layer, so that some transition dipole moments are still aligned parallel to the incoming light. Furthermore, extrapolating the isotropic absorbance shown in Fig. 4.10 using:

$$A_{\mathrm{iso}} = \frac{1}{3\left(A_{\parallel} + 2A_{\perp}\right)}, \tag{3.27}$$

the value of the coupling strength is 40 cm^{-1}, which is similar to that measured in Fig. 3.5d.

To extract the angular dependence of the Rabi splitting between the directrix of the molecule and $\mathbf{E}_0$, as expressed in Eq. 3.26, the average angle between $\hat{\mathbf{n}}$ and the molecular axis has to be determined. To do that, the order parameter S (Eq. 4.11) defined in Section 4.1.4 is used, and the experimental value of S is 0.60. Assuming an unimodal delta distribution around the tilt angle allows to rewrite Eq. 2.30 as follows:

$$\cos^2\theta = \frac{2}{3}(S+1), \tag{3.28}$$

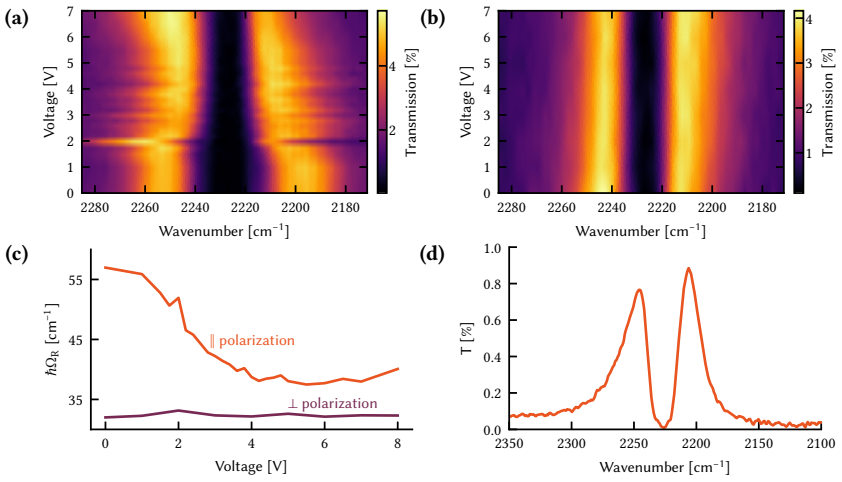

Figure 3.5 (a)-(b) Transmission maps of a cell as a function of the applied voltage for parallel and perpendicular polarisation, respectively. **(c)** Rabi splitting as a function of applied voltage for both polarisations. **(d)** Transmission spectrum isotropic 5CB inside a FP cavity, the value of $\hbar\Omega_R$ is 40 cm^{-1}.

yielding to $\theta = 31.2$. Using the value of θ the ratio between the coupling strength measured in the parallel and perpendicular cases can be predicted. Rewriting Eq. 3.26 as [1]:

$$\frac{\hbar\Omega_{R_\parallel}}{\hbar\Omega_{R_\perp}} = \frac{\boldsymbol{\mu}_\parallel \cdot \mathbf{E}_0}{\boldsymbol{\mu}_\perp \cdot \mathbf{E}_0} = \frac{\cos\theta}{\cos\left(\frac{\pi}{2} - \theta\right)} \frac{n_\parallel}{n_\perp}\,, \tag{3.29}$$

yields to a ratio of 1.81. The ratio $\frac{\hbar\Omega_{R_\parallel}}{\hbar\Omega_{R_\perp}}$ using the measured value from Fig. 3.5 gives a value of 1.78, hence confirming the calculated angle and thus the predicted value from Eq. 3.29. Moreover, the coupling strength has a square root relation to the molecular concentration, as discussed in the previous section, and the concentration is also linearly dependent to the molecular absorption through the Beer-Lambert-Bouguer law (Eq. 4.7). Those relations are verified through the ratio of their respective absorbance:

$$\sqrt{\frac{A_\parallel}{A_\perp}} = 1.75\,, \tag{3.30}$$

which agrees well with both the measured and predicted values.

In summary, it has been shown that liquid crystal molecules can be used for tuning the Rabi splitting by applying a voltage across the Fabry-Pérot cavity, hence an electrical switching in the strong coupling regime. The Rabi splitting switching ratio is 1.78, meaning that the orientational order induced by the liquid crystals increases the coupling strength by 41% compared to an isotropic phase.

3.3 Photophysical properties in the strong coupling regime

When an organic molecule is strongly coupled to an optical cavity, the relaxation pathways differ from the case of an isolate molecule, due to a change in the molecular electronic landscape. To investigate to which extent polaritonic states alters the excited state of a molecule, **Paper II** investigates the influence of strong-coupling on the process of intersystem crossing. To do so, the molecule Erythrosine B (ErB), which is the tetraiodide form of fluorescein (Fig. 3.6a), was put into strong coupling regime. Erb exhibits both fluorescence and phosphorescence at room temperature centered at 538 nm and 691 nm, respectively (Fig. 3.6b). Additionally, ErB exhibits an E-type delayed fluorescence at room temperature. E-type delayed fluorescence, also called thermally activated delayed fluorescence (TADF), is a process through which a triplet state can undergo a reverse intersystem crossing (i.e. $S_1 \longleftarrow T_1$) and then de-excite to the ground state through fluorescence.

Figure 3.6c displays the dispersion plot of a FP cavity filled with Erb showing a Rabi splitting of 375 meV. This corresponds to a lowering of the lower polariton energy of 135 meV compared to the absorption maximum of the S_1 state. The gradual lowering of the $|P^-\rangle$ state according to the coupling strength is shown in the emission spectra (Fig. 3.7a). Due to the Stokes shift of ErB, the energy difference between fluorescence and $|P^-\rangle$ emission is 135 meV. The phosphorescence band is independent of the coupling strength inside the FP cavity, hence emitting at the same energy than the uncoupled molecule, as shown in Fig. 3.7b.

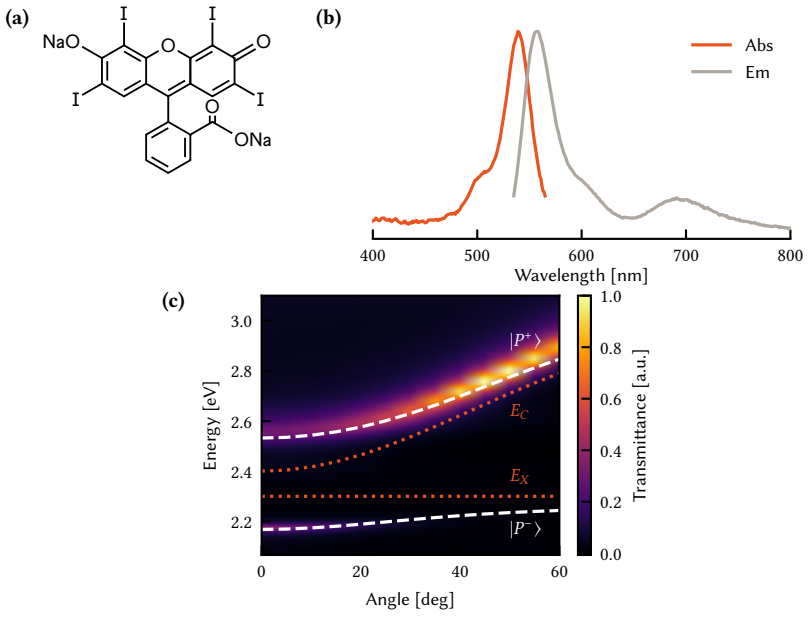

Figure 3.6 (a) Chemical structure of Erythrosine B. **(b)** Normalised absorption and emission of ErB thin film. **(c)** Angle-resolved transmission map of strongly coupled ErB in a FP cavity. The dashed white and orange dotted lines represent the coupled harmonic oscillator fitting of the data (Section 3.1.2).

Thus, the coupling of the S_1 state to the vacuum field does not affect the triplet states of the molecule. Therefore, the energy gap ΔE_{TS} between the $|\mathrm{P}^-\rangle$ and T_1 states can be selectively reduced by increasing the Rabi splitting.

Paper II shows how this effect can be used to increase in the rate of reverse intersystem crossing by lowering the energy gap between the lower polariton and the triplet state.

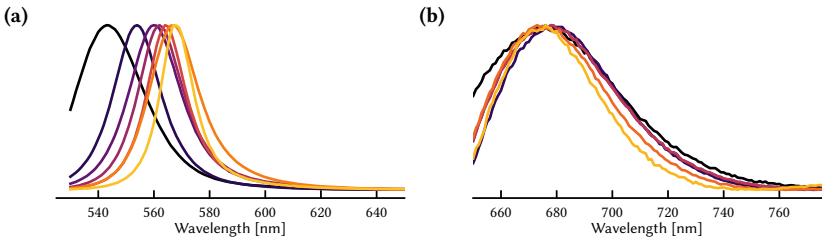

Figure 3.7 (a) Emission spectra of the lower polaritonic state. The color coding indicates the increases in molecular concentration (black to orange). **(b)** Phosphorescence of ErB using the same color coding than **(a)**.

3.4 Coupling strength enhancement using artificial plasmonic molecules

The Rabi splitting is limited by the molecular concentration inside a FP cavity. To overcome this limit and increase the coupling strength of strongly coupled systems in the IR, we investigated a FP cavity containing molecules as well as a periodic array of gold nanorods, as shown schematically in Fig. 3.8a. Two molecules were chosen for this investigation, hexanal and 4-butylbenzonitrile (Fig. 3.8b). The absorption band of the hexanal C = O stretch vibration is centered around 1724 cm^{-1} and the absorption band of the 4-butylbenzonitrile C ≡ N stretch vibration is located around 2225 cm^{-1}. Both absorption bands are sharp with a FWHM of 27 cm^{-1} and 10 cm^{-1}, respectively. The two molecules inside the FP cavity are in the strong coupling regime with a value of $\hbar\Omega_R$ of 101 cm^{-1} and 46 cm^{-1} for the C = O and C ≡ N bands, respectively.

The plasmon resonances were chosen to be on resonance with the vibrational absorption bands, as shown in the SEM pictures in Fig. 2.12. Figure 3.9a shows the FT-IR microscope transmission spectra of the gold arrays inside a FP cavity. As the length of the rods increases, the plasmon's resonances shift to lower energies providing a way of tuning the resonance condition. We observe a normal mode splitting of the bare plasmonic resonance, as well as a significant drop in the linewidth of the plasmonic bands (Table 3.1). This is due to the fact that in the IR the losses of the nanorods are dominated by radiative losses, but

Table 3.1 FWHM of the measured molecules, plasmons and cavities. All linewidths are given in cm^{-1} and rod lengths in nm.

media in cavity	air		hexanal		butylbenz
FP mode FWHM*	84 ± 7.3		42 ± 1.6		31.3 ± 2.9
Rod length [nm]	1100	1200	1300	1400	1500
Bare plasmon [cm^{-1}]	1120	1032	882	745	621
FP/rods polar. [cm^{-1}]	69.5 ± 0.5	72 ± 6	72.5 ± 0.5	66†	66†
FP/rods/hexanal polar. [cm^{-1}]	41.3 ± 7.4	41.3 ± 4.5	40.5 ± 2.5	36.3 ± 4.5	39.5 ± 1.5
FP/rods/butylbenz polar. [cm^{-1}]	34.3 ± 2.9	34 ± 2.8	33.5 ± 1.5	29 ± 4	/

* Measured next to the array
† Too much signal-to-noise to measure more than 1 peak

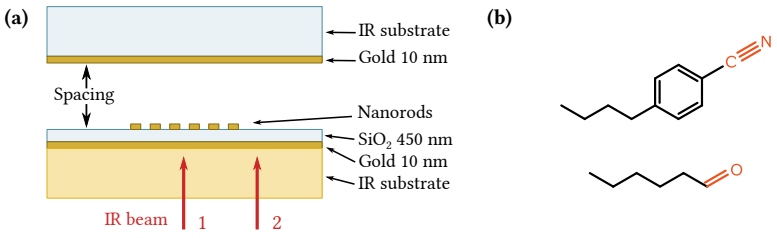

Figure 3.8 (a) Schematic figure of the FP cavity used in the study. The beams labeled 1 or 2 indicates the position where the cavity was probed using FT-IR microscopy, either on top, or next to, the nanorods array. **(b)** Chemical structure of 4-butylbenzonitrile (top) and hexanal (bottom).

inside a FP cavity, the radiation bounces back and forth between the mirrors, therefore reducing the resonance linewidth.

When introducing the molecules into the cavity with the gold array, a third component will couple with both the cavity and the plasmon. Figures 3.9b and 3.9c show the resulting transmission spectra, where the C = O absorption band is on resonance with the longest nanorods and the C ≡ N absorption band is on resonance with the shortest nanorods. To ensure that the dispersion spectra are indeed due to the interaction between the three components, transmission spectra with a polariser perpendicular to the rods' long axis were measured (Figs. 3.9d to 3.9f). The resulting spectra are the same than the spectra measured

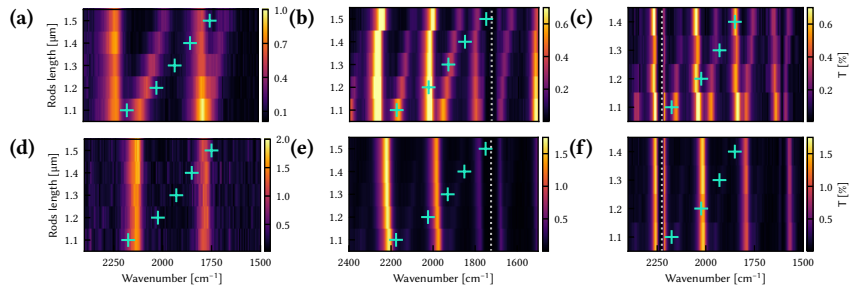

Figure 3.9 (a)-(c) Transmission maps of the plasmonic array inside the FP cavity, without molecules, with hexanal and with butylbenzonitrile, respectively. **(d)-(f)** Same transmission maps than before, but this time with a polarised light perpendicular to the long axis of the nanorods. The grey dashed line indicates the absorption band of the molecule and the green crosses indicate the absorption maximum of the bare plasmonic array.

without the plasmonic arrays.

Next, analytical modelling was performed to extract the coupling strengths of the hybrid cavity. To do so, the cavity can be described by M Fabry-Pérot eigenmodes with frequencies ω_m, each coupling to the vibrational absorption band of the molecules. Thus, the Jaynes-Cummings Hamiltonian is employed, which includes the M cavity modes:

$$\hat{H}_{mol} = \sum_{m=1}^{M} \hbar\omega_m \hat{a}_m^\dagger \hat{a}_m + \hbar\omega_0 \hat{b}^\dagger \hat{b} + \sum_{m=1}^{M} \hbar g_m \left(\hat{a}_m^\dagger \hat{b} + \hat{a}_m \hat{b}^\dagger \right) \tag{3.31}$$

Figure 3.10 shows the resulting fittings of the measured spectra. The coupling strength of the cavity containing the nanorods gives a value of $\hbar\Omega_R$ of 326 cm^{-1}, and when the molecules are inside the cavity, $\hbar\Omega_R$ is 396 cm^{-1} and 362 cm^{-1} for the C=O and C≡N absorption bands, respectively. In the cases where the molecules were inside the cavity, the plasmon and the molecules were modeled together as a single collective oscillator.

In summary, the nanorods and the molecules act together as a single collective oscillator, thus enhancing the total coupling strength of the system. Furthermore, the artificial plasmonic molecules increase the coupling strength of 4-butylbenzonitrile and hexanal by 9 and 5 times, respectively.

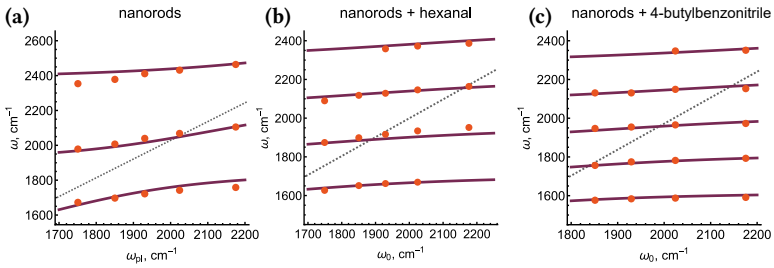

Figure 3.10 (a)-(c) Resulting fittings (purple line) of the measured transmission peaks (orange dots) from Fig. 3.9. The dotted lines indicates the absorption of the bare plasmonic arrays. ω_{pl} and ω_0 represent the plasmon and the plasmon+molecules frequencies, respectively.

CHAPTER 4

Methodology

[…] and thus render ourselves, as it were, masters and possessors of nature

René Descartes, Discourse on the Method

The next chapter describes the procedures and methods used during my doctoral studies. The chapter is divided into two sections, experimental and computational. We will begin to describe the basic principles of the optical characterisations used in this thesis, then the procedures used to put an organic molecule into the strong-coupling regime as well as computational methods used to characterise the experimental observations.

4.1 Experimental

What follows is an account of the experimental methods and techniques used in this thesis. First, we will give a brief overview of the spectroscopic techniques used to characterise Fabry-Pérot cavities, then the methods used to fabricate the optical cavities and finally the computational approach used to describe the experimental measurements.

4.1.1 Infrared spectroscopy

Infrared spectroscopy is based on the interaction between light and matter in the infrared range of the electromagnetic spectrum and is used to investigate vibrations and associated rotational-vibrational structures of organic and inorganic compounds.

The foundations of Fourier Transform-Infrared Spectroscopy (FT-IR) can be traced back to the end of the 19th century when Michelson developed and described an interferometer named after him [124, 125]. Subsequently, Lord Rayleigh published in 1892 a letter to Michelson relating the interferogram to the spectrum by using a Fourier transformation [126]. Peter Fellget, in 1949, was the first to transform an interferogram into an infrared spectrum [127]. Although the basis of modern FT-IR spectroscopy was developed, the computers available in the 1950s were not powerful enough to process the interferogram efficiently. A major breakthrough came in 1965 with the rediscovery of the Fast Fourier Transform algorithm (FFT) by Cooley and Tukey [128] (although discovered by Carl Friedrich Gauß in 1805 [129]) which improved the computation by an order of magnitude and was directly applied in optical interferometry by Forman in 1967 [130]. Few years later, mid-infrared FT-IR spectrometers were available and used to obtain rapid infrared spectra and are widely used today nanoscience to food science.

Principles of FT-IR spectroscopy

The main optical components of an FT-IR spectrometer (Fig. 4.1) are the following: an infrared light source, an interferometer consisting of one fixed mirror, one moving mirror and a beamsplitter, and an infrared detector [131].

The mid-infrared source (ca. 1.5 µm to 20 µm) is ideally a high temperature Planck radiator (i.e. a black-body). The most common mid-infrared source used, known as *Globar*, is a silicon carbide rod which is electrically heated up to ~1300 K. On the other side of the instrument, the detector is usually a thermal or a quantum detector. Thermal detectors operate by sensing the change in temperature of an absorbing material and then convert it into an

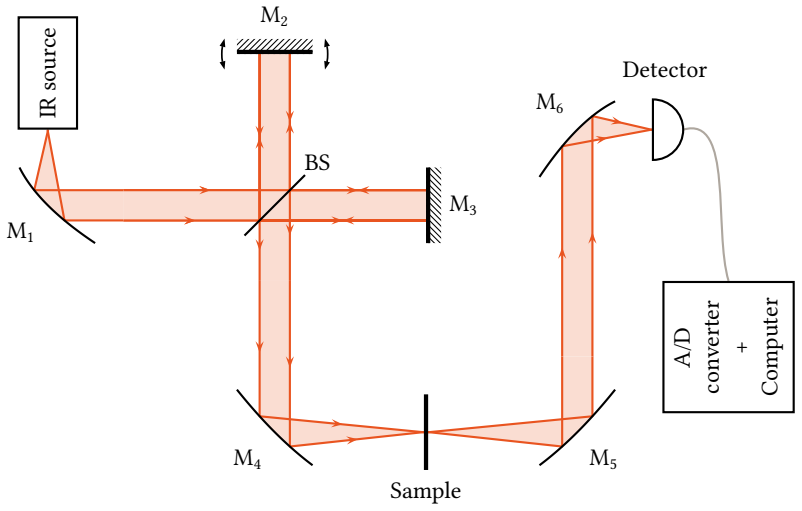

Figure 4.1 Optics of a common FT-IR spectrometer. M_1, M_4, M_5 and M_6 are off-axis parabolic mirrors of different focal lengths, M_2 and M_3 are the moving and fixed mirrors of the interferometer, BS is the interferometer beamsplitter and A/D is the analog-to-digital converter.

electrical signal, typically a voltage. Those detectors, operating at near room temperature, are pyroelectric bolometers and consist of temperature-sensitive ferroelectric crystals that exhibit a spontaneous electric polarization below their Curie temperature. Today many FT-IR instruments are equipped with a deuterated l-alanine-doped triglycine sulfate (DLaTGS) detector. When working with a low signal (e.g. when using a FT-IR microscope) it may be useful to use a quantum detector, such as the mercury cadmium telluride (MCT) detector. They are typically p-n junction semiconductors, and are based on the photoelectric effect. MCT detectors are usually cooled to 77 K with liquid nitrogen and offer a high signal-to-noise ratio and a fast response time.

At the heart of the FT-IR spectrometer is the interferometer based on a two-beam interferometer originally designed by Michelson. The interferometer is used to split the infrared beam from the source into two beams in order to give

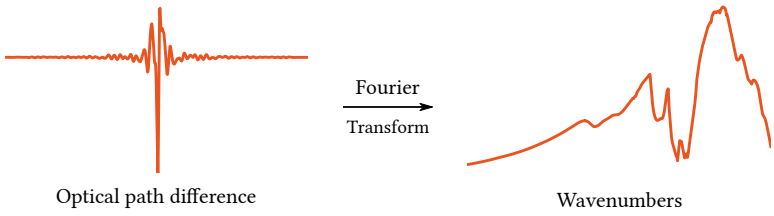

Figure 4.2 Interferogram before the Fourier transformation resulting in a power spectrum. The unit of the optical path difference is cm and the power spectrum is cm^{-1}.

the two beams a different path. When the two beams come out from the interferometer, an interferogram is generated, i.e. the signal produced as a function of the change of path length between the two beams. Then the signal passes through the sample and reaches the detector before being converted to a digital form by an analog-to-digital converter. The recorded signal is interconvertible to a power spectrum by a Fourier transformation defined as [132]:

$$I(x) = \int_{-\infty}^{\infty} E(\nu)\, e^{2\pi i \nu x}\, \mathrm{d}\nu \tag{4.1a}$$

$$E(\nu) = \int_{-\infty}^{\infty} I(x)\, e^{-2\pi i \nu x}\, \mathrm{d}x\,, \tag{4.1b}$$

where, $I(x)$ is the intensity of the interferogram, x is the optical path difference, $E(x)$ is the intensity of the spectrum and ν is the wavenumber. The Fourier transformation of an interferogram yields a power spectrum, as shown in Fig. 4.2. Finally, the power spectrum of a measured sample is ratioed with the background spectrum to obtain the final absorption or transmission spectrum.

Attenuated total reflectance spectroscopy

Attenuated total reflectance (ATR) was developed in the early 1960s by Harrick [133] and Fahrenfort [134] and makes use of the principle of total internal reflection. The reflection at the interface between two media of different refractive indices is describe by the Snell-Descartes law, or commonly known as the Snell's

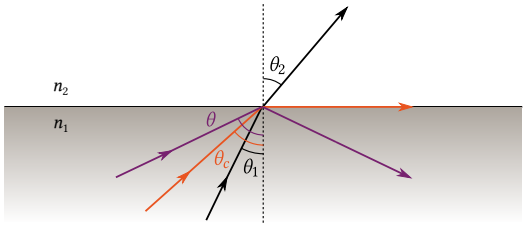

Figure 4.3 Illustration of Snell's law. All angle are measured between the incident (or refracted) ray and the surface normal.

law [135]:

$$n_1 \sin \theta_1 = n_2 \sin \theta_2 \,, \tag{4.2}$$

where n_1 and n_2 are the refractive indices of the medium 1 and 2, respectively, θ_1 is the angle of incidence and θ_2 is the angle of refraction. When the incident light originates from an optically dense medium, with a refractive index $n_1 > n_2$, the angle of incidence θ_1 will be smaller than the angle of refraction θ_2 (Fig. 4.3). According to the Snell's law (Eq. 4.2) the angle of incidence is always smaller than the refracted one, so if θ_1 is increased to a specific angle, called the critical angle θ_c, the beam will propagate along the interface. The value of the critical angle is the value of θ_1 for which $\theta_2 = \frac{\pi}{2}$:

$$\theta_c = \arcsin\left(\frac{n_2}{n_1}\right) . \tag{4.3}$$

Besides, when $\theta > \theta_c$ the beam cannot propagate into the medium with the lower refractive index, it is totally reflected inside the material. Any material that exhibits internal reflection is referred to as internal reflection element (IRE).

Although the whole beam is totally reflected, there is an electromagnetic wave beyond the interface that penetrates a short distance into the low refractive index medium. This extended wave is referred to as evanescent wave. The intensity of the evanescent wave decreases exponentially with distance above the interface between the two media. At the interface, the electric field penetrates perpendicularly into the optically thinner medium n_2. The amplitude $\mathbf{E}$ of the

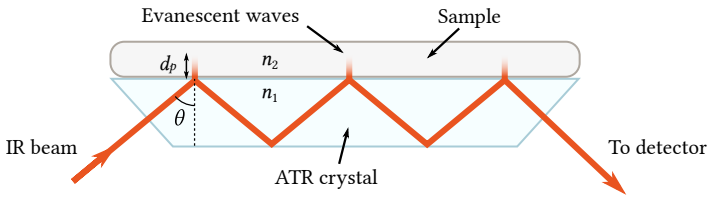

Figure 4.4 Illustration of an ATR crystal, typically diamond, with a sample in contact with the IRE, showing the penetration of the infrared beam into the sample.

electric field as a function of the distance z from the IRE is given by:

$$\mathbf{E} = \mathbf{E_0} e^{-\gamma z}, \tag{4.4}$$

where, $\mathbf{E_0}$ is the electric field amplitude at the interface and γ is a decay constant. Thus, when an absorbing material is placed on the surface of the optically dense material, it will interact with the evanescent wave to generate a spectrum. This is called attenuated total reflectance. The distance over which the evanescent wave can interact with the absorbing material is dependent of the wavelength of the incident beam and the refractive indices of the two media. The distance from the interface where the electric field amplitude $\mathbf{E}$ of the evanescent wave is decreased by a value of e^{-1} is called the penetration depth d_p and is given by [131]:

$$d_p = \frac{\lambda_1}{2\pi n_1 \sqrt{\sin^2\theta - \left(\frac{n_2}{n_1}\right)^2}}, \tag{4.5}$$

where, λ_1 is the wavelength of the optically dense material and is related to the incident infrared beam by the expression $\lambda_1 = \lambda/n_1$. The depth of penetration is typically a few microns (ca. 0.5 µm to 3 µm) depending on the refractive index of the IRE and the angle of incidence.

After internal reflection, the infrared beam exits the IRE and is going to the detector. A typical ATR setup is shown in Fig. 4.4. The sample requires very little preparation as long as sufficient contact area between the sample and the IRE is attained. Attenuated total reflectance is today widely used as a non destructive technique applied for liquid and solid samples.

FT-IR microscopy

A FT-IR microscope is a hyphenated technique combining a FT-IR spectrometer with an optical microscope. The beam coming from the interferometer is focused onto the sample, in most microscopes, by a Cassegrain condenser, which consists of a small convex mirror suspended above a larger concave mirror. After transmitting through the sample, the beam is collected by another Cassegrain condenser, the objective, and sent to a liquid nitrogen cooled MCT detector at which the interferogram is recorded. The spatial resolution is an important feature in the application of FT-IR microscopy. The spatial resolution of the microscope is based on the minimum distance r at which two measurements points can be distinguished, known as the Rayleigh criterion. The spatial resolution is defined as follows [131]:

$$r = \frac{0.61\lambda}{\mathrm{NA}}, \tag{4.6}$$

where, λ is the wavelength and NA is the numerical aperture of the Cassegrain.

In infrared microscopes, the infrared beam is around few hundreds of microns at the focal point, and the measured sample is often smaller than the beam diameter. Consequently, not the whole beam does interact with the sample, this is called stray light. This is why an adjustable aperture, consisting of knife edges, is placed on top of the objective to reduce the diameter of the beam. Therefore, only the infrared radiation that has interacted with the sample is recorded into the detector.

FT-IR microscopy allows measuring infrared spectra as small as 10 µm and provides physical and chemical informations on samples such as size, shape, morphology, chemical composition as well as mapping a region of a complex heterogeneous sample [136].

4.1.2 Ultraviolet-visible spectroscopy

Ultraviolet-visible (UV-Vis) spectroscopy is routinely used to get insights of fundamental informations of molecules, such as atomic and molecular energy levels, electronic transitions, or molecular geometry [137, 138]. Absorbance in

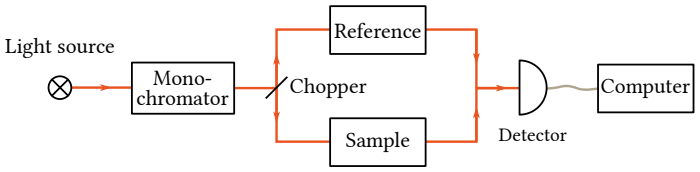

Figure 4.5 Instrumental design of a double beam UV-Vis spectrophotometer.

every spectral range of the electromagnetic field depends on the Beer-Lambert-Bouguer law, commonly known as the Beer's law:

$$A(\lambda) = \varepsilon(\lambda) c \ell \,, \tag{4.7}$$

where, $A(\lambda)$ is the absorbance, $\varepsilon(\lambda)$ is the molar absorptivity, c is the concentration of the absorbing compound and ℓ is the pathlength. The spectrophotometer does not measure the absorbance directly, but extracts it from the quantity of light transmitted through the sample. This is known as the transmittance and is given by:

$$T = \frac{I}{I_0} \,, \tag{4.8}$$

where, T is the transmittance, I_0 the intensity of light transmitted without the absorbing material and I the intensity of the light passing through the sample. The final absorbance is related to the transmittance by:

$$A = -\log(T) = \log\left(\frac{I_0}{I}\right) \,. \tag{4.9}$$

The basic architecture of a spectrophotometer consists of one or more light sources, a monochromator, a detector and a computer (Fig. 4.5). Most of modern spectrophotometer are based on a double-beam design. The incoming beam from the light source is separated in two by a rotating mirror that directs the beam first through the reference path and then through the sample. The light sources are often a deuterium arc lamp for the ultraviolet part of the electromagnetic spectrum (ca. 190 nm to 320 nm) and a tungsten filament lamp for the visible to near infrared (ca. 320 nm to 2500 nm). The combination of those two lamps

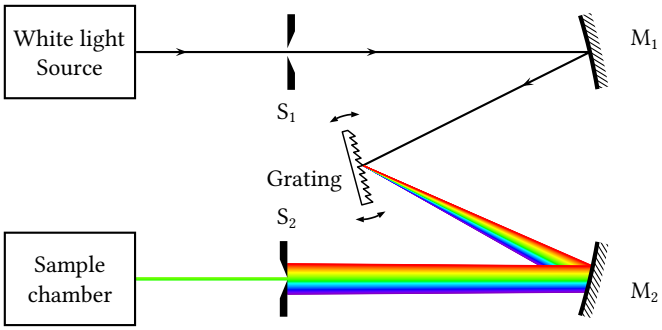

Figure 4.6 Optical diagram of a Czerny-Turner monochromator. S_1 and S_2 are the entrance and exit slits, respectively, M_1 and M_2 are curved mirrors. The diffraction grating rotates in order to select which wavelength of the light exits the monochromator.

provides a continuous spectrum in the UV-Vis region of the electromagnetic spectrum.

Subsequently the light passes through a wavelength selector, which selects specific and narrow wavelengths prior to measurements. This is done by a monochromator. Figure 4.6 shows the principle of a diffraction grating monochromator. The most commonly used monochromator is the Czerny-Turner design where the light enters through an entrance slit and is reflected into the grating with a curved mirror. The diffracted light is then reflected by another curved mirror before going out through the exit slit, that allows only one specific wavelengths to pass through, and going to the sample chamber.

Thereafter, the light reaches the detector, a transducer which converts the light into an electrical signal. This is typically done with a photomultiplier tube (PMT). First, the incoming photon is absorbed on a photoemissive material, the photocathode, that emits free electrons. The electrons are then accelerated by a high voltage (typically few hundreds of volts) to a first electrode, called dynode, where they generate several secondary electrons. Those are accelerated towards further dynodes, where the number of emitted electrons is getting order of

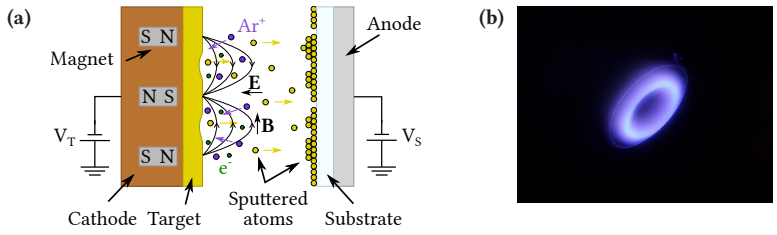

Figure 4.7 (a) Schematic diagram of a planar magnetron. **(b)** Photograph of a magnetron plasma on top of a gold target.

magnitudes larger each time. The amplified photocurrent is then collected with an anode before being processed and converted to a spectrum by a computer. PMT's are sensitive detectors to measure low amounts of light and are widely used in modern spectrophotometer.

4.1.3 Thin film deposition

The section below describes the basic principles to deposit thin films, in particular the metallic thin films used as mirrors as well the thin polymer layers used for aligning the liquid crystals.

Direct current magnetron sputtering

Direct current (DC) magnetron sputtering is a widely-used physical vapor deposition (PVD) method for the deposition of metallic thin films [139, 140]. DC magnetron sputtering is a high vacuum ionic sputtering method, where high energy ions bombard a target and eject atoms from the surface (shown schematically in Fig. 4.7a). The role of the magnetron is to enhance the ionization of the argon atoms by introducing a magnetic field in the vicinity of the target by placing magnets below the target. The cloud of electrons and ions created on the front of the target is denoted as the magnetron plasma.

To ignite the magnetron discharge, a high DC voltage (ca. 500 V) is applied. When argon is introduced in the vacuum chamber, it will ionise and create a plasma, where electrons and ions are separated. The free electrons will be

affected by a force **F**, given by the Lorentz force:

$$\mathbf{F} = q(\mathbf{E} + \mathbf{v} \times \mathbf{B}), \tag{4.10}$$

where, q is the electric charge, **E** the electrical field, **v** the velocity and **B** the magnetic field. Due to the geometry of the magnetic field (parallel to the target), electrons are trapped in the $\mathbf{E} \times \mathbf{B}$ drift current and will enhance the probability of ionising the argon gas. Once the plasma is ignited, the Ar^+ ions are accelerated to the negatively charged target, thus bombarding the target and ejecting the material towards the substrate (Fig. 4.7b). The thickness and the rate of deposition are monitored with a quartz crystal microbalance (QCM), which measures the change in frequency of a piezoelectric quartz crystal. The change in frequency is then correlated to the mass change on the surface of the crystal.

In summary, DC magnetron sputtering is a thin film coating technique providing a high deposition rate, high purity deposition and excellent adhesion on the substrate, and was used in this thesis to make thin films of Ag, Au and ITO.

Spin-coating

Having discussed how to deposit metallic thin films, the next section addresses the basic principle of organic thin film deposition using the spin-coating technique. Spin-coating is a thin film deposition technique where a liquid solution is deposited on top of a flat substrate and then spreaded by centrifugal force [141]. The process of spin-coating can be described in four steps (shown schematically in Fig. 4.8). First a thick layer of molecules dissolved in a volatile solvent is deposited on the substrate (step 1). Then the chuck starts to rotate (step 2) at high speed (> 600 rpm) which spreads the liquid in a viscous flow (step 3). Finally, an airflow induced by the high spinning speed will evaporate the solvent leaving the molecules on the surface of the substrate (step 4).

By adjusting the spinning speed, the acceleration rate and the solvent, a uniform and precise film thickness can be achieved with spin-coating.

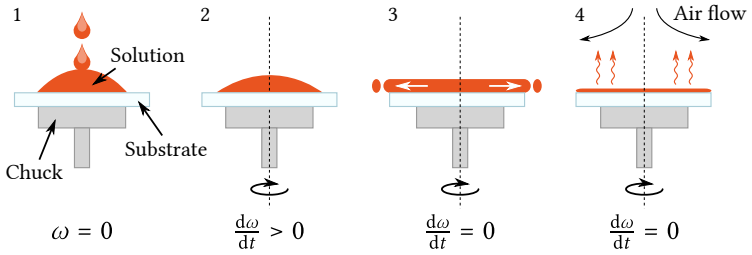

Figure 4.8 Schematic principle of the spin-coating process. Here ω is the angular speed.

4.1.4 Liquid crystals alignment

A common method used to achieve homogeneous alignment, where the alignment of the director vector has a preferred direction within the plane of the substrate, is the so-called rubbing technique [142]. To do so, a polymer thin film is spin-coated onto the substrate and then rubbed with a velvet cloth a few times in one direction. The rubbing process will reorient the long chains of the polymer layer, creating nano-grooves in the direction of the rubbing. Consequently, when the liquid crystals are in close contact with the polymer layer, the director will align parallel (or perpendicular) to the grooves in order to minimise the elastic energy [143] (although the mechanism is not well understood), hence achieving homogeneous planar alignment.

In the study presented in **Paper I**, the liquid crystal (LC) used is the well-known 5CB (4-Cyano-4'-pentylbiphenyl, Fig. 4.9a), which exhibits a nematic phase at room temperature. In order to align the liquid crystal inside the cell, the following procedure was used. Inside a cleanroom, 0.1% polyimide (PI2610) dissolved in dimethyl sulfoxide (DMSO) was spin-coated at 5000 rpm for 30 seconds onto the substrates, yielding to a 20 nm thick layer. A soft bake at 100 °C for one minute was done to evaporate the solvent before curing in a convection oven at 300 °C for 3 hours with a ramp rate of 4 °C min^{-1} in order to obtain an insoluble polyimide film and to remove residual solvent. The substrates were rubbed unidirectionally in a buffing machine (LC-tec AB, Borlänge, Sweden)

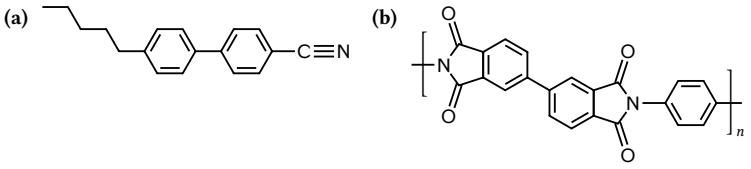

Figure 4.9 (a) Chemical structure of the liquid crystal 5CB. **(b)** Chemical structure of PI2610 polymer.

using a velvet cloth in order to give the boundary condition for the self-alignment to the LCs.

To verify if the liquid crystals are aligned, one way is to relate the order parameter S (Section 2.2) to an infrared absorption dichroism measurement. Using this method, the order parameter is determined by [94]:

$$S = \frac{gD - 1}{gD + 2} \frac{1}{1 - \frac{3}{2}\sin^2\beta}, \tag{4.11}$$

where, g is a correction factor originating from the anisotropy of the local field of the incident light, D is the dichroic ratio and β is the angle between the long axis and the transition dipole moment of the LC. While both g and β are properties from the LCs, the dichroic ratio D is measured from polarised absorption bands, and is defined as:

$$D = \frac{A_\parallel}{A_\perp}, \tag{4.12}$$

where $A_\parallel$ and $A_\perp$ are the parallel and perpendicular polarised IR absorbances, respectively. Figure 4.10 shows the absorption of the C≡N stretching vibration of 5CB under polarised light as well as the extracted value of the order parameter S from **Paper I**. The extracted value of S is 0.60 which means that the LCs inside the cell are aligned. This section has described how to align liquid crystals inside a cell, and the next section will describe how to switch and control the orientation of the liquid crystals inside the cell.

4.1.5 Electro-optic switching of liquid crystals

To control the orientation of the liquid crystals inside the cell (Section 2.2.1), an external electric field is applied across the cell. To do so, an infrared transparent

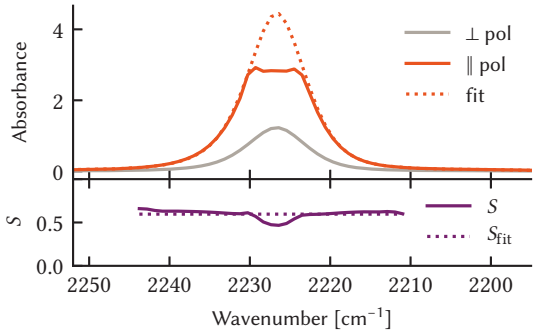

Figure 4.10 Absorbance spectra of aligned 5CB liquid crystal with parallel (orange) and perpendicular (grey) polarisation. The dotted orange line is a fit of the absorption spectrum to extrapolate the high absorbance. The bottom plot is the extracted order parameter S using Eq. 4.11.

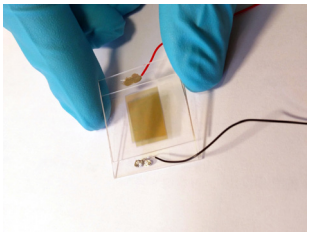

Figure 4.11 Photograph of a processed 5CB microcavity.

conductive layer is deposited onto the substrates. Then a voltage is applied between the two mirrors to generate a electric field across the cell, which will distort the uniformly aligned liquid crystals.

In **Paper I**, to apply an electric field across the LC cell, 100 nm of indium-tin oxide (ITO, In_2O_3-SnO_2 90–10 wt%) was deposited onto the substrate using a DC magnetron sputter system at a deposition rate of 1.07 Å s^{-1}. Directly after deposition, the substrates were baked at 400 °C on a hot plate to improve the conductivity of the ITO layer. Finally, electrical wires were soldered on the ITO layer using a conductive silver paste. Fig. 4.11 shows a processed LC cell made of two CaF_2 substrates, an IR transparent crystal, ITO layers, sputtered gold mirrors in the middle and the electrical wires.

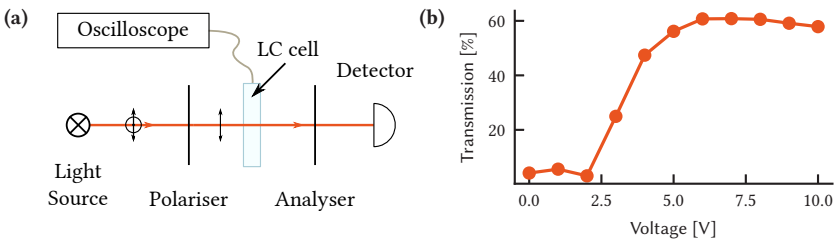

Figure 4.12 (a) Diagram of the cross-polarised setup. Here the two polariser are oriented 90° towards each others. **(b)** Transmission spectrum resulting from the cross-polarised setup showing the Fréedericksz transition around 3 V.

To switch the orientation of the LCs inside the cell, a square signal of 1 kHz is applied, and measured (peak to peak), using a signal generator coupled to an oscilloscope. In order to check if the LCs is properly switching a linear crossed polarised setup was build (Fig. 4.12a). If the liquid crystals are in an homogeneous phase, the incoming linear polarised light will not be affected, therefore no light will be transmitted because the analyser has a polarisation angle of 90° compared to the first polariser. When an electric field is applied the nematic LCs will undergo a splay-type transition and will twist to an homeotropic phase, hence affecting the plane of polarisation of the transmitted light. Figure 4.12b shows the transition between those two phases, hence confirming the re-orientation of the liquid crystals inside the cell.

4.1.6 Cavity thickness adjustment

Precise control of the thickness of the Fabry-Pérot cavity is crucial to all experiments involving strong light-matter interaction, due to the fact that both the molecular transition (electronic or vibrational) and the cavity must be on resonance. To control the thickness of the cavities designed in this thesis, different approaches were used.

In **Paper I**, the liquid crystal cell was made by gluing two CaF_2 substrates together, where poly(methyl methacrylate) (PMMA) microspheres where dis-

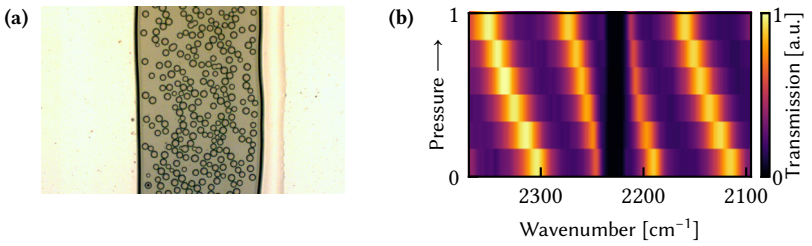

Figure 4.13 (a) Photograph of the PMMA microspheres in the glue. The diameter of the largest sphere is 32 µm. **(b)** Transmission map of a 5CB Fabry-Pérot cavity with an applied mechanical pressure on the cavity.

persed inside the glue to give a nominal thickness of 32 µm. The thickness of the cell was determined using the following equation:

$$d = \frac{m}{2n}\left(\frac{\lambda_1\lambda_2}{\lambda_1 - \lambda_2}\right), \tag{4.13}$$

where m is the number of resonance peaks, n the refractive index, and λ_1 and λ_2 the wavelength of the peaks. Then to fine tune the physical distance between the mirrors, a mechanical pressure was applied to the cavity. Figure 4.13 shows the PMMA microspheres dispersed in the glue used to seal the LC cell and shows the fine tuning of the cavity resonance when a mechanical pressure is applied onto the cavity.

In **Paper III** and **Paper IV**, the thickness was controlled using BoPET (biaxially-oriented polyethylene terephthalate) films, known as *Mylar*, or using PTFE (polytetrafluoroethylene) films having a nominal thickness of 6, 12, 25 or 50 µm. The design of the FP cavities in these two studies were different than in **Paper I**, as molecules in liquid state were studied. They were fabricated using a demountable cell made for infrared spectroscopy (Omni Cell, Specac). The two gold mirrors were coated onto IR transparent substrate and closed together. The thickness was then finely tuned using adjustment screws on the microfluidics cell, using the same mechanical pressure principle as in **Paper I**.

Finally, in **Paper II**, the Fabry-Pérot cavity is on resonance with a molecular electronic transition, thus micrometer spacers cannot be used to control the distance between the mirrors. The cavity thickness was adjusted by spin-coating

the molecules dispersed in a polymer matrix. By adjusting different parameters (e.g. polymer type, density, spin-coating speed) the desired thickness was achieved.

4.2 Computational

So far this chapter has focused on the experimental techniques used in this thesis. The following section will discuss the computational techniques employed. This section will first describe the transfer matrix method (TMM) used to characterise the optical properties of the microcavities built during my doctoral studies, then the approach used to extract the complex refractive index of the materials used in the microcavities.

The transfer matrix method, the Drude-Lorentz and the Lorentzian relations fittings were implemented using Scipy [144], Numpy [145], Matplotlib [146] Python packages on Python 3.7, and the Kramers-Kronig relations were computed using Octave 5.1 [147]. Other fitting routines used, such as the coupled harmonic oscillator model described in Section 3.1.2, are based on the LMFIT Python package [148].

4.2.1 Transfer matrix method

The optical cavities presented in this thesis can be modelled as a one dimensional (1D) multilayer structure, i.e. a sum of 1D optically isotropic and homogeneous layers. Their coherent optical properties, such as transmission and reflection, can be computed using a transfer matrix method [135, 149, 150]. This method is a simple and powerful tool, used for example, to study organic solar cells [151], organic light emitting devices [152] as well as perovskite multilayer structures [153].

The basic concept of the TMM is to solve the famous Maxwell's equation in a multilayer system for an uniform incoming electric field **E**. As a starting point

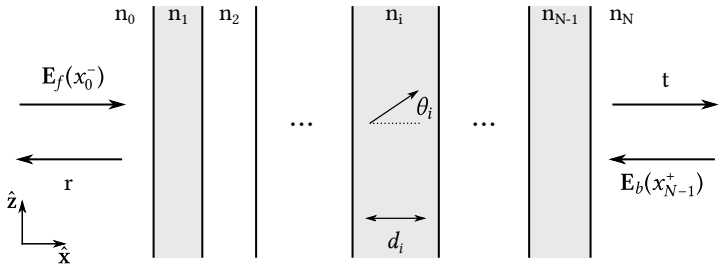

Figure 4.14 Schematic figure of the multilayered structure. The first and last layer are semi-infinite layer.

the Maxwell's equations in vacuum are used [135]:

$$\begin{aligned} \nabla \times \mathbf{E} &= -\frac{\partial \mathbf{B}}{\partial t} & \nabla \cdot \mathbf{B} &= 0 \\ \nabla \times \mathbf{B} &= \mu_0 \varepsilon_0 \frac{\partial \mathbf{E}}{\partial t} & \nabla \cdot \mathbf{E} &= 0\,, \end{aligned} \tag{4.14}$$

where $\mathbf{E}$ is the electric field, $\mathbf{B}$ is the magnetic field, μ_0 is the vacuum permeability and ε_0 is the vacuum permittivity. The multilayer structure consists of a stack of layered media with thickness d_i and refractive indices n_i, all separated by interface planes (Fig. 4.14). Thus we can model the multilayer structure as a system with one input and one output $\mathbf{E}$ field. Consequently, a transfer matrix $\widetilde{M}$ can be computed to relate the incident and reflected waves at input with the incident and reflected waves at the other side of the multilayer structure. If the matrix $\widetilde{M}$ is known, the transmitted and reflected electromagnetic fields can be calculated for an interface between two layers. Then by multiplying the individual transfer matrices, the total transfer matrix is obtained and the final transmission and reflection of the system is computed.

Let's look in more details how to derive the final transmission or reflection of a multilayer structure. The problem is splitted in two, one for the the TE-polarisation ($\mathbf{E}$ parallel to the interfaces) and for the TM-polarisation ($\mathbf{B}$ parallel to the interfaces). Thus, the electric field is entirely described by its amplitude $\mathbf{E}(\mathbf{r})$. Moreover, the total electric field at a position $\mathbf{r}$ within a layer is described

as a superposition of the forward and backward propagating plane wave:

$$\mathbf{E}(\mathbf{r}) = \mathbf{E}_f e^{i\mathbf{k}_f \cdot \mathbf{r}} + \mathbf{E}_b e^{i\mathbf{k}_b \cdot \mathbf{r}}, \tag{4.15}$$

where $\mathbf{E}_f$ and $\mathbf{E}_b$ are the forward and backward wave amplitudes. The wave vectors $\mathbf{k}_f$ and $\mathbf{k}_b$ are related to the refractive index n_i by:

$$\begin{aligned} \mathbf{k}_f &= \frac{2\pi n_i}{\lambda} (\hat{\mathbf{z}} \cos\theta + \hat{\mathbf{x}} \sin\theta) \\ \mathbf{k}_b &= \frac{2\pi n_i}{\lambda} (-\hat{\mathbf{z}} \cos\theta + \hat{\mathbf{x}} \sin\theta), \end{aligned} \tag{4.16}$$

where, λ is the wavelength and θ the angle to the normal of the layer. It should be noted that $\mathbf{k}_{f,b}$ can be a complex number and that its imaginary part is nonzero if the wave propagates in a lossy medium (see Section 4.2.2). The transfer matrix $\widetilde{M}$ relates to the complex amplitude $\mathbf{E}_f$ and $\mathbf{E}_b$ just before (x^-) and after (x^+) the first and last layers of the structure. The general relation is defined as:

$$\begin{pmatrix} \mathbf{E}_f(x_0^-) \\ \mathbf{E}_b(x_0^-) \end{pmatrix} = \widetilde{M} \begin{pmatrix} \mathbf{E}_f(x_{N-1}^+) \\ \mathbf{E}_b(x_{N-1}^+) \end{pmatrix} = \begin{pmatrix} \widetilde{M}_{00} & \widetilde{M}_{01} \\ \widetilde{M}_{10} & \widetilde{M}_{11} \end{pmatrix} \begin{pmatrix} \mathbf{E}_f(x_{N-1}^+) \\ \mathbf{E}_b(x_{N-1}^+) \end{pmatrix}. \tag{4.17}$$

Now let's build the transfer matrices for wave propagation through a layer and between an interface before calculating the complete transfer matrix $\widetilde{M}$ by a multiplication of all individual ones. The transfer matrix for a wave propagating between a layer i and j relating the forward and backward propagating waves is given by the scattering matrix S_{ij} of the interface between the two layers:

$$\begin{pmatrix} \mathbf{E}_f(x_i^+) \\ \mathbf{E}_b(x_i^-) \end{pmatrix} = S_{ij} \begin{pmatrix} \mathbf{E}_f(x_i^-) \\ \mathbf{E}_b(x_i^+) \end{pmatrix} = \begin{pmatrix} t_{ij} & r_{ji} \\ r_{ij} & t_{ji} \end{pmatrix} \begin{pmatrix} \mathbf{E}_f(x_i^-) \\ \mathbf{E}_b(x_i^+) \end{pmatrix}, \tag{4.18}$$

where t_{ij} and r_{ij} are the complex transmission and reflection coefficients of the incident wave at the interface. They are known as the complex Fresnel coefficients and are derived from the Snell's law (Eq. 4.2). For the TE-polarisation, the Fresnel coefficients are given by [135]:

$$r_{ij} = \frac{\mathbf{E}_b(x_i^-)}{\mathbf{E}_f(x_i^-)} = \frac{n_i \cos\theta_i - n_j \cos\theta_j}{n_i \cos\theta_i + n_j \cos\theta_j} \tag{4.19a}$$

$$t_{ij} = \frac{\mathbf{E}_f(x_i^+)}{\mathbf{E}_f(x_i^-)} = 1 + r_{ij} = \frac{2n_i \cos\theta_i}{n_i \cos\theta_i + n_j \cos\theta_j}, \tag{4.19b}$$

and for the TM-polarisation:

$$r_{ij} = \frac{\mathbf{E}_b(x_i^-)}{\mathbf{E}_f(x_i^-)} = \frac{n_j \cos\theta_i - n_i \cos\theta_j}{n_j \cos\theta_i + n_i \cos\theta_j} \tag{4.20a}$$

$$t_{ij} = \frac{\mathbf{E}_f(x_i^+)}{\mathbf{E}_f(x_i^-)} = \frac{n_i}{n_j}(1 + r_{ij}) = \frac{2n_i \cos\theta_i}{n_i \cos\theta_j + n_j \cos\theta_i} . \tag{4.20b}$$

We can now rewrite Eq. 4.18 to relate $\mathbf{E}_{f,b}(x_i^-)$ and $\mathbf{E}_{f,b}(x_i^+)$:

$$\begin{pmatrix} \mathbf{E}_f(x_i^-) \\ \mathbf{E}_b(x_i^-) \end{pmatrix} = \begin{pmatrix} \frac{1}{t_{ij}} & -\frac{r_{ji}}{t_{ij}} \\ \frac{r_{ij}}{t_{ij}} & t_{ji} - \frac{r_{ij}}{t_{ij}} r_{ji} \end{pmatrix} \begin{pmatrix} \mathbf{E}_f(x_i^+) \\ \mathbf{E}_b(x_i^+) \end{pmatrix} . \tag{4.21}$$

Making use of the symmetry relations of the Fresnel coefficients, $r_{ij} = -r_{ji}$ and $t_{ij}t_{ji} - r_{ij}r_{ji} = 1$, Eq. 4.21 becomes:

$$\begin{pmatrix} \mathbf{E}_f(x_i^-) \\ \mathbf{E}_b(x_i^-) \end{pmatrix} = \frac{1}{t_{ij}} \begin{pmatrix} 1 & r_{ij} \\ r_{ij} & 1 \end{pmatrix} \begin{pmatrix} \mathbf{E}_f(x_i^+) \\ \mathbf{E}_b(x_i^+) \end{pmatrix} . \tag{4.22}$$

Therefore, the transfer matrix M_{ij} for a wave propagating between interface i and j is obtained and reads:

$$M_{ij} = \frac{1}{t_{ij}} \begin{pmatrix} 1 & r_{ij} \\ r_{ij} & 1 \end{pmatrix} . \tag{4.23}$$

Now, let's move on to building the transfer matrix M_j for a wave propagating through a layer j. The relations between the waves before and after an interface for the forward and backward propagating waves are given by:

$$\mathbf{E}_f(x_j^-) = \mathbf{E}_f(x_{j-1}^+)\, e^{i\delta_j} = \mathbf{E}_f(x_{j-1}^+)\, e^{i\frac{2\pi}{\lambda} n_j d_j \cos\theta_j} \tag{4.24a}$$

$$\mathbf{E}_b(x_{j-1}^+) = \mathbf{E}_b(x_j^-)\, e^{i\delta_j} = \mathbf{E}_b(x_j^-)\, e^{i\frac{2\pi}{\lambda} n_j d_j \cos\theta_j} , \tag{4.24b}$$

where, δ_j represents the phase shift angle experimented by the wave after passing layer j, d_j is the thickness of layer j and n_j the complex refractive index of layer j. Thus, the transfer matrix M_j propagating into layer j reads:

$$M_j = \begin{pmatrix} e^{-i\delta_j} & 0 \\ 0 & e^{i\delta_j} \end{pmatrix} . \tag{4.25}$$

We can now build the transfer matrix T_j between two layers j and $j+1$ by multiplying the interface matrix $M_{j,j+1}$ and the propagation matrix M_j:

$$T_j = M_{j,j+1} M_j = \frac{1}{t_{j,j+1}} \begin{pmatrix} 1 & r_{j,j+1} \\ r_{j,j+1} & 1 \end{pmatrix} \begin{pmatrix} e^{-i\delta_j} & 0 \\ 0 & e^{i\delta_j} \end{pmatrix} . \tag{4.26}$$

Hence, the complete transfer matrix $\widetilde{M}$ for a wave propagating through a structure of N layers is obtained by multiplying all the individual transfer matrices:

$$\widetilde{M} = \begin{pmatrix} 1 & r_{0,1} \\ r_{0,1} & 1 \end{pmatrix} \frac{1}{t_{0,1}} \prod_{j=1}^{N-1} T_j . \tag{4.27}$$

Considering a normalised incident wave (i.e. $\mathbf{E}_f(x_0^-) = 1$) and no wave coming from the right side (Fig. 4.14), i.e. $\mathbf{E}_b(x_{N-1}^+) = 0$, of the multilayer structure, we can rewrite Eq. 4.17 in the following way:

$$\begin{pmatrix} 1 \\ \mathbf{E}_b(x_0^-) \end{pmatrix} = \widetilde{M} \begin{pmatrix} \mathbf{E}_f(x_{N-1}^+) \\ 0 \end{pmatrix} = \begin{pmatrix} \widetilde{M}_{00} & \widetilde{M}_{01} \\ \widetilde{M}_{10} & \widetilde{M}_{11} \end{pmatrix} \begin{pmatrix} \mathbf{E}_f(x_{N-1}^+) \\ 0 \end{pmatrix} . \tag{4.28}$$

This leads to the the final reflection and transmission coefficient of the layered structure:

$$t = \mathbf{E}_b(x_0^-) = \frac{1}{\widetilde{M}_{00}} \tag{4.29a}$$

$$r = \mathbf{E}_f(x_{N-1}^+) = \frac{\widetilde{M}_{10}}{\widetilde{M}_{00}} . \tag{4.29b}$$

The final reflectance R and transmittance T of the multilayer structure is derived from the radiant flux density I (or irradiance) given by [135]:

$$I = \langle S \rangle_t = \frac{1}{2Z_0} |\mathbf{E}_0|^2 . \tag{4.30}$$

where $\langle S \rangle_t$ is the time-averaged magnitude of the Poynting vector, Z_0 the vacuum impedance ($\sqrt{\mu_0/\varepsilon_0}$) and $\mathbf{E}_0$ the amplitude of the electric field. This represents the average energy per unit of time crossing a unit area normal to the Poynting vector ($\mathbf{S} = c^2 \varepsilon_0 \, \mathbf{E} \times \mathbf{B}$). Let I_i, I_r and I_t be the incident, reflected and transmitted flux density, respectively. We can define the reflectance R and the transmittance

T as the ratio of the reflected flux and transmitted flux, respectively, to the incident flux [135]:

$$\begin{aligned} R &\equiv \frac{I_t}{I_i} \\ T &\equiv \frac{I_t \cos\theta}{I_i \cos\theta_0} \,. \end{aligned} \tag{4.31}$$

Finally, applying Eqs. 4.30 and 4.31 to the final layer (with no backward light in the final layer), one obtains the reflectance and transmittance, for all polarisations, of the multilayered structure as a function of Eqs. 4.29a and 4.29b:

$$T_{\mathrm{TE}} = |t|^2 \frac{\mathrm{Re}(n\cos\theta)}{\mathrm{Re}(n_0\cos\theta_0)} \tag{4.32a}$$

$$T_{\mathrm{TM}} = |t|^2 \frac{\mathrm{Re}(n\cos\bar{\theta})}{\mathrm{Re}(n_0\cos\bar{\theta}_0)} \tag{4.32b}$$

$$R = |r|^2 \,. \tag{4.32c}$$

By implementing Eqs. 4.2, 4.19, 4.20, 4.27, 4.29 and 4.32 into a computer code, and solving these equations for each wavelength and angle, the simulated optical spectra measured in **Papers II–III** are computed. To fully simulate the optical properties of a multilayer structure, the only input parameters needed are the wavelength and angle of the incident light, the thicknesses of the layers and their complex refractive indices. In the next section, we will describe how to obtain the complex refractive index of thin metallic layers and organic thin films.

4.2.2 Complex refractive index

Having discussed how to construct the transfer matrix method, the final section of this thesis addresses ways of extracting the complex refractive index of thin films. In order to compute the optical properties of a multilayer structure using a transfer matrix approach (Section 4.2.1), we must determine the complex refractive index of the lossy medium. The wavelength dependent complex refractive index $\tilde{n}(\lambda)$ is defined as [135, 154]:

$$\tilde{n}(\lambda) \equiv n(\lambda) + i\kappa(\lambda) \tag{4.33}$$

where κ is the extinction coefficient, which is non-zero for an absorbing material. In this thesis, we used two different techniques to extract the complex refractive index from absorption measurements: the Kramers-Kronig relations and the Drude-Lorentz relation.

Kramers-Kronig relations

To obtain the complex refractive index, the extinction coefficient κ can be extracted from absorption measurements. The relation between the extinction coefficient and the measured absorbance is derived from Beer's law (Eq. 4.7) and given by:

$$\kappa(\lambda) = \frac{\alpha(\lambda)\lambda}{4\pi} = \frac{A(\lambda)\lambda}{4\pi d}\ln(10)\,, \tag{4.34}$$

where, α is the attenuation coefficient, A the absorbance and d the thickness of the layer. Now that the imaginary part of the refractive index is determined, we can obtain the real part of $\tilde{n}$ by using the famous Kramers-Kronig (KK) relations. Those relations were derived from Kronig's work on dispersion theory applied on X-rays [155] and Kramers' work showing that the principle of causality allows the calculation of the real refractive index of a medium from the absorption spectrum [156].

In short, the complex refractive index $\tilde{n}$ is a holomorphic function in the upper half plane (i.e. positive imaginary part: $\{x + iy \mid y > 0; x, y \in \mathbb{R}\}$), hence a Hilbert transform can be applied to relate the extinction coefficient to the real refractive index, known as the KK dispersion relations, and defined as [154, 157, 158]:

$$n(\omega) - 1 = \frac{2}{\pi}\mathcal{P}\int_0^\infty \frac{\omega'\kappa(\omega')}{\omega'^2 - \omega^2}\,\mathrm{d}\omega' \tag{4.35a}$$

$$\kappa(\omega) = -\frac{2\omega}{\pi}\mathcal{P}\int_0^\infty \frac{n(\omega') - 1}{\omega'^2 - \omega^2}\,\mathrm{d}\omega'\,, \tag{4.35b}$$

where, $\mathcal{P}$ is the Cauchy principal value and ω the frequency. This allows to extract the dispersion relation of an organic thin film from absorption (or transmission) measurements. This method was used in **Paper II** in order to simulate the

angle-resolved transmission spectrum, using the TMM approach, of Erythrosine B inside a Fabry-Pérot cavity.

Infrared optical constants

In order to extract the optical constants of the gold mirrors used in **Paper III**, a Drude-Lorentz model was used. The complex dielectric function $\tilde{\varepsilon}(\omega)$ can be expressed as a sum of the dielectric functions of the free-electron effects (intraband effects) and the bound-electron effects (interband effects) at a given frequency ω [135, 159, 160]:

$$\tilde{\varepsilon}(\omega) = \varepsilon_{\text{free}}(\omega) + \varepsilon_{\text{bound}}(\omega)\,. \tag{4.36}$$

The free-electron part is expressed using a Drude model and reads:

$$\varepsilon_{\text{free}}(\omega) = 1 - \frac{f_0\omega_p^2}{\omega(\omega - i\gamma_0)}\,, \tag{4.37}$$

where, f_0 is the oscillator strength of the intraband transition, ω_p is the plasma frequency, which describes the oscillations of electrons, and γ_0 is the damping constant. The second term in the complex dielectric function arises from the bound electrons and is given by the Lorentz model describing the response of an isotropic dielectric medium subjected to an applied electric field. For each oscillators f_j having a resonant frequency ω_j, with a corresponding damping rate γ_j, the dielectric function of the bound electrons reads:

$$\varepsilon_{\text{bound}}(\omega) = \sum_{j=1}^{m} \frac{f_j\omega_p^2}{\omega_j^2 - \omega^2 + i\omega\gamma_j}\,. \tag{4.38}$$

Using the Maxwell's relation for the refractive index in a medium (assuming a non magnetic material at optical frequency) $n = \sqrt{\varepsilon_r\mu_r} \approx \sqrt{\varepsilon_r}$, one obtains the complex refractive index of the gold mirrors:

$$\begin{aligned} n(\omega) &= \text{Re}\left(\sqrt{\tilde{\varepsilon}(\omega)}\right) \\ \kappa(\omega) &= \text{Im}\left(\sqrt{\tilde{\varepsilon}(\omega)}\right)\,. \end{aligned} \tag{4.39}$$

Thus using Eq. 4.33, we can extract the optical constants of gold and use them in the TMM simulation to characterise a multilayer system.

In order to obtain the optical response of an organic compound in the infrared region a multi-Lorentz oscillator model was used, and is given by [160, 161]:

$$\tilde{n}(k) = \sqrt{n_b^2 - \sum_{j=0}^{N} \frac{f_j}{k^2 - k_{0j}^2 + ik\gamma_j}} \,. \tag{4.40}$$

where, n_b is the background refractive index, f_j is the oscillator strength, k_{0j} is the resonant wave vector and γ_j is the damping constant, i.e. the full width at half maximum of the j^{th} oscillator. Using Eq. 4.40 to fit the infrared spectrum of a compound, we can extract its complex refractive index by taking the real and imaginary part of Eq. 4.40.

CHAPTER 5

Summary of Research & Outlook

Prediction is very difficult, especially about the future

ATTRIBUTED TO NIELS BOHR

Strong light-matter interaction is a phenomenon where light and matter interact within a confined electromagnetic field in resonance with the molecular transition. Consequently, two new hybrid states, known as polaritonic states will emerge. This thesis focuses on the study of molecular properties in the strong coupling regime as well as developing new methods to increase the coupling strength between light and matter.

To maximise the effect provided by the polaritonics states in chemistry and material sciences, a high coupling strength is required, as shown by theoretical studies. In this thesis, we have shown that aligning the molecular transition dipole moment to the confined electric field increases the Rabi splitting by almost 50% using liquid crystal molecules. The same technique has been used in the visible range achieving huge coupling strengths [49]. Additionally, a hierarchical coupling between a Fabry-Pérot cavity, a localised surface plasmon resonance and a vibrational absorption band is demonstrated. Such system shows almost an order of magnitude increase in the total coupling strength for a nitrile absorption band, and can easily be integrated into microfluidic devices in which

vibropolaritonic chemical reactions have been performed [162]. Microfluidics' integration is crucial for applications, therefore planar microcavities must be upscaled to a length scale used in flow chemistry, without reducing the coupling strength. In this spirit, we have shown that a typical Fabry-Pérot cavity can be upscaled without reducing the interaction between light and matter.

Furthermore, exploring the consequences of strong light-matter interaction on photophysical properties are of importance to solve the challenges that our society is facing, such as developing energy efficient organic light emitting devices or organic lasers without organometallic complexes known for their high costs and toxicity [163]. Selective manipulation of excited states in strong coupling regime are demonstrated.

Since the start of my PhD in 2016, the field of vibrational strong coupling has grown from just a few seminal papers in 2015 [164–167] to astonishing developments [122, 168–188]. This opens up an important area of multidisciplinary research that goes back more than forty years. Vibropolaritonic chemistry is rapidly emerging as an exciting field and much has to be done to unleash the full potential of polaritonic states, for example a chemical reaction in a vibrational Bose-Einstein condensate.

Bibliography

[1] Hertzog, M., Rudquist, P., Hutchison, J. A., George, J., Ebbesen, T. W., and Börjesson, K., "Voltage-controlled switching of strong light–matter interactions using liquid crystals", Chem. Eur. J. **23**, 18166–18170 (2017).

[2] Stranius, K., Hertzog, M., and Börjesson, K., "Selective manipulation of electronically excited states through strong light–matter interactions", Nat. Commun. **9**, 2273 (2018).

[3] Hertzog, M. and Börjesson, K., "The effect of coupling mode in the vibrational strong coupling regime", ChemPhotoChem **4**, 612–617 (2020).

[4] Bahsoun, H., Chervy, T., Thomas, A., Börjesson, K., Hertzog, M., George, J., Devaux, E., Genet, C., Hutchison, J. A., and Ebbesen, T. W., "Electronic light–matter strong coupling in nanofluidic Fabry–Pérot cavities", ACS Photonics **5**, 225–232 (2018).

[5] Mony, J., Hertzog, M., Kushwaha, K., and Börjesson, K., "Angle-independent polariton emission lifetime shown by perylene hybridized to the vacuum field inside a Fabry–Pérot cavity", J. Phys. Chem. C **122**, 24917–24923 (2018).

[6] Hertzog, M., Wang, M., Mony, J., and Börjesson, K., "Strong light–matter interactions: a new direction within chemistry", Chem. Soc. Rev. **48**, 937–961 (2019).

[7] Cravcenco, A., Hertzog, M., Ye, C., Iqbal, M. N., Mueller, U., Eriksson, L., and Börjesson, K., "Multiplicity conversion based on intramolecular triplet-to-singlet energy transfer", Sci. Adv. **5**, eaaw5978 (2019).

[8] Zubairy, M. S., "A very brief history of light", in *Optics in our time* (Springer, 2016), pp. 3–24.

[9] Dirac, P. A. M. and Bohr, N. H. D., "The quantum theory of the emission and absorption of radiation", Proc. R. Soc. Lond. A **114**, 243–265 (1927).

[10] Nelson, J., *The physics of solar cells* (Imperial College Press, 2003).

[11] Dougherty, T. J., Gomer, C. J., Henderson, B. W., Jori, G., Kessel, D., Korbelik, M., Moan, J., and Peng, Q., "Photodynamic therapy", JNCI Journal of the National Cancer Institute **90**, 889–905 (1998).

[12] Anderson, P. W., "More is different", Science **177**, 393–396 (1972).

[13] Hestand, N. J. and Spano, F. C., "Expanded theory of H- and J-molecular aggregates: the effects of vibronic coupling and intermolecular charge transfer", Chem. Rev. **118**, 7069–7163 (2018).

[14] Simpson, W. T. and Peterson, D. L., "Coupling strength for resonance force transfer of electronic energy in van der Waals solids", J. Chem. Phys. **26**, 588–593 (1957).

[15] Kasha, M., Rawls, H. R., and El-Bayoumi, M. A., "The exciton model in molecular spectroscopy", Pure Appl. Chem. **11**, 371–392 (1965).

[16] Drexhage, K. H., "IV interaction of light with monomolecular dye layers", in *Progress in optics* (Elsevier, 1974), pp. 163–232.

[17] Yakovlev, V., Nazin, V., and Zhizhin, G., "The surface polariton splitting due to thin surface film LO vibrations", Opt. Commun. **15**, 293–295 (1975).

[18] Pockrand, I., Brillante, A., and Möbius, D., "Exciton–surface plasmon coupling: an experimental investigation", J. Chem. Phys. **77**, 6289–6295 (1982).

[19] Deng, H., Weihs, G., Santori, C., Bloch, J., and Yamamoto, Y., "Condensation of semiconductor microcavity exciton polaritons", Science **298**, 199–202 (2002).

[20] Kasprzak, J. et al., "Bose–Einstein condensation of exciton polaritons", Nature **443**, 409–414 (2006).

[21] Balili, R., Hartwell, V., Snoke, D., Pfeiffer, L., and West, K., "Bose-Einstein condensation of microcavity polaritons in a trap", Science **316**, 1007–1010 (2007).

[22] Amo, A. et al., “Collective fluid dynamics of a polariton condensate in a semiconductor microcavity”, Nature **457**, 291–295 (2009).

[23] Carusotto, I. and Ciuti, C., “Quantum fluids of light”, Rev. Mod. Phys. **85**, 299–366 (2013).

[24] Karzig, T., Bardyn, C.-E., Lindner, N. H., and Refael, G., “Topological polaritons”, Phys. Rev. X **5**, 031001 (2015).

[25] Tsutsui, T., Takada, N., Saito, S., and Ogino, E., “Sharply directed emission in organic electroluminescent diodes with an optical-microcavity structure”, Appl. Phys. Lett. **65**, 1868–1870 (1994).

[26] Nakayama, T. and Kakuta, A., “Organic luminescent devices with a multiplex cavity structure”, Jpn. J. Appl. Phys. **34**, L1234–L1236 (1995).

[27] Tessler, N., Denton, G. J., and Friend, R. H., “Lasing from conjugated-polymer microcavities”, Nature **382**, 695–697 (1996).

[28] Lidzey, D. G., Bradley, D. D. C., Pate, M. A., David, J. P. R., Whittaker, D. M., Fisher, T. A., and Skolnick, M. S., “Mapping the confined optical field in a microcavity via the emission from a conjugated polymer”, Appl. Phys. Lett. **71**, 744–746 (1997).

[29] Lidzey, D. G., Bradley, D. D. C., Skolnick, M. S., Virgili, T., Walker, S., and Whittaker, D. M., “Strong exciton–photon coupling in an organic semiconductor microcavity”, Nature **395**, 53–55 (1998).

[30] Agranovich, V., Benisty, H., and Weisbuch, C., “Organic and inorganic quantum wells in a microcavity: Frenkel-Wannier-Mott excitons hybridization and energy transformation”, Solid State Commun. **102**, 631–636 (1997).

[31] Hobson, P. A., Barnes, W. L., Lidzey, D. G., Gehring, G. A., Whittaker, D. M., Skolnick, M. S., and Walker, S., “Strong exciton–photon coupling in a low-Q all-metal mirror microcavity”, Appl. Phys. Lett. **81**, 3519–3521 (2002).

[32] Lidzey, D. G., Fox, A. M., Rahn, M. D., Skolnick, M. S., Agranovich, V. M., and Walker, S., "Experimental study of light emission from strongly coupled organic semiconductor microcavities following nonresonant laser excitation", Phys. Rev. B **65**, 195312 (2002).

[33] Dintinger, J., Klein, S., Bustos, F., Barnes, W. L., and Ebbesen, T. W., "Strong coupling between surface plasmon-polaritons and organic molecules in subwavelength hole arrays", Phys. Rev. B **71**, 035424 (2005).

[34] Wenus, J., Ceccarelli, S., Lidzey, D. G., Tolmachev, A. I., Slominskii, J. L., and Bricks, J. L., "Optical strong coupling in microcavities containing J-aggregates absorbing in near-infrared spectral range", Org. Electron. **8**, 120–126 (2007).

[35] Schwartz, T., Hutchison, J. A., Genet, C., and Ebbesen, T. W., "Reversible switching of ultrastrong light-molecule coupling", Phys. Rev. Lett. **106**, 196405 (2011).

[36] Hutchison, J. A., Liscio, A., Schwartz, T., Canaguier-Durand, A., Genet, C., Palermo, V., Samorì, P., and Ebbesen, T. W., "Tuning the work-function via strong coupling", Adv. Mater. **25**, 2481–2485 (2013).

[37] Coles, D. M., Somaschi, N., Michetti, P., Clark, C., Lagoudakis, P. G., Savvidis, P. G., and Lidzey, D. G., "Polariton-mediated energy transfer between organic dyes in a strongly coupled optical microcavity", Nat. Mater. **13**, 712–719 (2014).

[38] Coles, D. M., Yang, Y., Wang, Y., Grant, R. T., Taylor, R. A., Saikin, S. K., Aspuru-Guzik, A., Lidzey, D. G., Tang, J. K.-H., and Smith, J. M., "Strong coupling between chlorosomes of photosynthetic bacteria and a confined optical cavity mode", Nat. Commun. **5**, 5561 (2014).

[39] George, J., Wang, S., Chervy, T., Canaguier-Durand, A., Schaeffer, G., Lehn, J.-M., Hutchison, J. A., Genet, C., and Ebbesen, T. W., "Ultra-strong coupling of molecular materials: spectroscopy and dynamics", Faraday Discuss. **178**, 281–294 (2015).

[40] Orgiu, E. et al., "Conductivity in organic semiconductors hybridized with the vacuum field", Nat. Mater. **14**, 1123–1129 (2015).

[41] Chervy, T. et al., "High-efficiency second-harmonic generation from hybrid light-matter states", Nano Lett. **16**, 7352–7356 (2016).

[42] Zhong, X., Chervy, T., Wang, S., George, J., Thomas, A., Hutchison, J. A., Devaux, E., Genet, C., and Ebbesen, T. W., "Non-radiative energy transfer mediated by hybrid light-matter states", Angew. Chem. Int. Ed. **55**, 6202–6206 (2016).

[43] Zhong, X., Chervy, T., Zhang, L., Thomas, A., George, J., Genet, C., Hutchison, J. A., and Ebbesen, T. W., "Energy transfer between spatially separated entangled molecules", Angew. Chem. Int. Ed. **129**, 9162–9166 (2017).

[44] Coles, D. et al., "A nanophotonic structure containing living photosynthetic bacteria", Small **13**, 1701777 (2017).

[45] Cookson, T. et al., "A yellow polariton condensate in a dye filled microcavity", Adv. Opt. Mater. **5**, 1700203 (2017).

[46] Georgiou, K., Michetti, P., Gai, L., Cavazzini, M., Shen, Z., and Lidzey, D. G., "Control over energy transfer between fluorescent BODIPY dyes in a strongly coupled microcavity", ACS Photonics **5**, 258–266 (2017).

[47] Munkhbat, B., Wersäll, M., Baranov, D. G., Antosiewicz, T. J., and Shegai, T., "Suppression of photo-oxidation of organic chromophores by strong coupling to plasmonic nanoantennas", Sci. Adv. **4**, eaas9552 (2018).

[48] Chervy, T., Azzini, S., Lorchat, E., Wang, S., Gorodetski, Y., Hutchison, J. A., Berciaud, S., Ebbesen, T. W., and Genet, C., "Room temperature chiral coupling of valley excitons with spin-momentum locked surface plasmons", ACS Photonics **5**, 1281–1287 (2018).

[49] Roux, F. L., Taylor, R. A., and Bradley, D. D. C., "Enhanced and polarization-dependent coupling for photoaligned liquid crystalline conjugated polymer microcavities", ACS Photonics **7**, 746–758 (2020).

[50] Chervy, T., Knüppel, P., Abbaspour, H., Lupatini, M., Fält, S., Wegscheider, W., Kroner, M., and Imamoğlu, A., "Accelerating polaritons with external electric and magnetic fields", Physical Review X **10**, 011040 (2020).

[51] Thomas, P. A., Tan, W. J., Fernandez, H. A., and Barnes, W. L., "A new signature for strong light–matter coupling using spectroscopic ellipsometry", Nano Lett., 10.1021/acs.nanolett.0c01963 (2020).

[52] Nagarajan, K. et al., "Conductivity and photoconductivity of a p-type organic semiconductor under ultrastrong coupling", ACS Nano, 10.1021/acsnano.0c03496 (2020).

[53] Herrera, F. and Spano, F. C., "Absorption and photoluminescence in organic cavity QED", Phys. Rev. A **95**, 053867 (2017).

[54] Martínez-Martínez, L. A., Ribeiro, R. F., Campos-González-Angulo, J., and Yuen-Zhou, J., "Can ultrastrong coupling change ground-state chemical reactions?", ACS Photonics **5**, 167–176 (2017).

[55] Luk, H. L., Feist, J., Toppari, J. J., and Groenhof, G., "Multiscale molecular dynamics simulations of polaritonic chemistry", J. Chem. Theory Comput. **13**, 4324–4335 (2017).

[56] Feist, J., Galego, J., and Garcia-Vidal, F. J., "Polaritonic chemistry with organic molecules", ACS Photonics **5**, 205–216 (2017).

[57] Herrera, F. and Spano, F. C., "Theory of nanoscale organic cavities: the essential role of vibration-photon dressed states", ACS Photonics **5**, 65–79 (2017).

[58] Sáez-Blázquez, R., Feist, J., Fernández-Domínguez, A. I., and García-Vidal, F. J., "Organic polaritons enable local vibrations to drive long-range energy transfer", Phys. Rev. B **97**, 241407 (2018).

[59] Ribeiro, R. F., Martínez-Martínez, L. A., Du, M., Campos-Gonzalez-Angulo, J., and Yuen-Zhou, J., "Polariton chemistry: controlling molecular dynamics with optical cavities", Chem. Sci. **9**, 6325–6339 (2018).

[60] Galego, J., Climent, C., Garcia-Vidal, F. J., and Feist, J., "Cavity casimir-polder forces and their effects in ground-state chemical reactivity", Phys. Rev. X **9**, 021057 (2019).

[61] Mandal, A. and Huo, P., "Investigating new reactivities enabled by polariton photochemistry", J. Phys. Chem. Lett. **10**, 5519–5529 (2019).

[62] Climent, C., Galego, J., Garcia-Vidal, F. J., and Feist, J., "Plasmonic nanocavities enable self-induced electrostatic catalysis", Angew. Chem. Int. Ed. **58**, 8698–8702 (2019).

[63] Csehi, A., Vibók, Á., Halász, G. J., and Kowalewski, M., "Quantum control with quantum light of molecular nonadiabaticity", Phys. Rev. A **100**, 053421 (2019).

[64] Campos-Gonzalez-Angulo, J. A., Ribeiro, R. F., and Yuen-Zhou, J., "Resonant catalysis of thermally activated chemical reactions with vibrational polaritons", Nat. Commun. **10**, 4685 (2019).

[65] Csehi, A., Kowalewski, M., Halász, G. J., and Vibók, Á., "Ultrafast dynamics in the vicinity of quantum light-induced conical intersections", New J. Phys. **21**, 093040 (2019).

[66] Phuc, N. T., Trung, P. Q., and Ishizaki, A., "Controlling the nonadiabatic electron-transfer reaction rate through molecular-vibration polaritons in the ultrastrong coupling regime", Sci. Rep. **10**, 7318 (2020).

[67] Gu, B. and Mukamel, S., "Cooperative conical intersection dynamics of two pyrazine molecules in an optical cavity", J. Phys. Chem. Lett. **11**, 5555–5562 (2020).

[68] Ulusoy, I. S. and Vendrell, O., "Dynamics and spectroscopy of molecular ensembles in a lossy microcavity", J. Chem. Phys. **153**, 044108 (2020).

[69] Gu, B. and Mukamel, S., "Manipulating nonadiabatic conical intersection dynamics by optical cavities", Chem. Sci. **11**, 1290–1298 (2020).

[70] Fregoni, J., Corni, S., Persico, M., and Granucci, G., "Photochemistry in the strong coupling regime: a trajectory surface hopping scheme", J. Comput. Chem. **41**, 2033–2044 (2020).

[71] Mandal, A., Krauss, T. D., and Huo, P., "Polariton-mediated electron transfer via cavity quantum electrodynamics", J. Phys. Chem. B **124**, 6321–6340 (2020).

[72] Fregoni, J., Granucci, G., Persico, M., and Corni, S., "Strong coupling with light enhances the photoisomerization quantum yield of azobenzene", Chem **6**, 250–265 (2020).

[73] Einstein, A., "Über einen die erzeugung und verwandlung des lichtes betreffenden heuristischen gesichtspunkt", Ann. Phys. **322**, 132–148 (1905).

[74] Lewis, G. N., "The conservation of photons", Nature **118**, 874–875 (1926).

[75] Landau, L. and Lifshitz, E., *Quantum mechanics: non-relativistic theory* (Pergamon Press, Oxford New York, 1977).

[76] Peter Atkins, J. d. P., *Atkins' physical chemistry* (Oxford University Press, Mar. 2014).

[77] Morse, P. M., "Diatomic molecules according to the wave mechanics. II. vibrational levels", Phys. Rev. **34**, 57–64 (1929).

[78] Hollas, J. M., *Modern spectroscopy* (John Wiley & Sons Inc, Nov. 2003), 482 pp.

[79] Vien, D., *The handbook of Infrared and Raman characteristic frequencies of organic molecules* (Academic Press, Boston, 1991).

[80] Daniel C. Harris, M. D. B., *Symmetry and spectroscopy: an introduction to vibrational and electronic spectroscopy* (Dover Publications, 1989), 576 pp.

[81] Willock, D., *Molecular symmetry* (John Wiley & Sons Inc, 2009).

[82] Atkins, P., Paula, J. de, and Friedman, R., *Quanta, matter, and change: a molecular appraoch to physical change* (W. H. Freeman, Nov. 2008), 782 pp.

[83] Pauli, W., "Über den zusammenhang des abschlusses der elektronengruppen im atom mit der komplexstruktur der spektren", Z. Physik **31**, 765–783 (1925).

[84] Kasha, M., "Characterization of electronic transitions in complex molecules", Discuss. Faraday Soc. **9**, 14 (1950).

[85] Dirac, P. A. M. and Fowler, R. H., "The quantum theory of the electron", Proc. R. Soc. Lond. A **117**, 610–624 (1928).

[86] Atkins, P. W., *Molecular quantum mechanics* (Oxford University Press, New York, 2005).

[87] El-Sayed, M. A., "Spin-orbit coupling and the radiationless processes in nitrogen heterocyclics", J. Chem. Phys. **38**, 2834–2838 (1963).

[88] Englman, R. and Jortner, J., "The energy gap law for radiationless transitions in large molecules", Mol. Phys. **18**, 145–164 (1970).

[89] Valeur, B., *Molecular fluorescence: principles and applications* (Wiley-VCH, Weinheim New York, 2002).

[90] Friedel, G., "Les états mésomorphes de la matiè re", Annales de Physique **9**, 273–474 (1922).

[91] Gennes, P. de and Prost, J., *The physics of liquid crystals* (Clarendon Press Oxford University Press, Oxford New York, 1993).

[92] Saupe, A. and Maier, W., "Methoden zur bestimmung des ordnungsgrades nematischer kristallinflüssiger schichten", Z. Naturforsch **16**, 816–824 (1961).

[93] Fréedericksz, V. and Zolina, V., "Forces causing the orientation of an anisotropic liquid", Trans. Faraday Soc. **29**, 919–930 (1933).

[94] Wu, S.-T., "Infrared markers for determining the order parameters of uniaxial liquid crystals", Appl. Opt. **26**, 3434 (1987).

[95] Kelly, K. L., Coronado, E., Zhao, L. L., and Schatz, G. C., "The optical properties of metal nanoparticles: the influence of size, shape, and dielectric environment", J. Phys. Chem. B **107**, 668–677 (2003).

[96] Barnes, W. L., "Particle plasmons: why shape matters", Am. J. Phys **84**, 593–601 (2016).

[97] Rodriguez, S., Schaafsma, M., Berrier, A., and Rivas, J. G., "Collective resonances in plasmonic crystals: size matters", Physica B **407**, 4081–4085 (2012).

[98] Kravets, V. G., Kabashin, A. V., Barnes, W. L., and Grigorenko, A. N., "Plasmonic surface lattice resonances: a review of properties and applications", Chem. Rev. **118**, 5912–5951 (2018).

[99] Auguié, B. and Barnes, W. L., "Collective resonances in gold nanoparticle arrays", Phys. Rev. Lett. **101**, 143902 (2008).

[100] Chu, Y., Schonbrun, E., Yang, T., and Crozier, K. B., "Experimental observation of narrow surface plasmon resonances in gold nanoparticle arrays", Appl. Phys. Lett. **93**, 181108 (2008).

[101] Auguié, B. and Barnes, W. L., "Diffractive coupling in gold nanoparticle arrays and the effect of disorder", Opt. Lett. **34**, 401 (2009).

[102] Lockhart, A. B., Skinner, A., Newman, W., Steinwachs, D. B., and Hilbert, S. A., "An experimental demonstration of avoided crossings with masses on springs", Am. J. Phys **86**, 526–530 (2018).

[103] Newman, W., Skinner, A., and Hilbert, S. A., "An acoustic demonstration of an avoided crossing", Am. J. Phys **85**, 844–849 (2017).

[104] Riek, C., Seletskiy, D. V., Moskalenko, A. S., Schmidt, J. F., Krauspe, P., Eckart, S., Eggert, S., Burkard, G., and Leitenstorfer, A., "Direct sampling of electric-field vacuum fluctuations", Science **350**, 420–423 (2015).

[105] Planck, M., "Eine neue strahlungshypothese", Werh. Dtsch. Phys. Ges. **13**, 138–148 (1911).

[106] Einstein, A. and Stern, O., "Einige argumente für die annahme einer molekularen agitation beim absoluten nullpunkt", Ann. Phys. **345**, 551–560 (1913).

[107] Nernst, W., "Über einen versuch von quantentheoretischen betrachtungen zur annahme stetiger energieänderungen zurückzukehren", Werh. Dtsch. Phys. Ges. **18**, 83–116 (1916).

[108] Casimir, H. B., "On the attraction between two perfectly conducting plates", Proc. Kon. Ned. Akad. Wet. **51**, 793 (1948).

[109] Serge Haroche, J.-M. R., *Exploring the quantum: atoms, cavities, and photons* (Oxford University Press, 2013), 616 pp.

[110] Jaynes, E. and Cummings, F., "Comparison of quantum and semiclassical radiation theories with application to the beam maser", Proc. IEEE **51**, 89–109 (1963).

[111] Dicke, R. H., "Coherence in spontaneous radiation processes", Phys. Rev. **93**, 99–110 (1954).

[112] Garraway, B. M., "The Dicke model in quantum optics: Dicke model revisited", Phil. Trans. R. Soc. A **369**, 1137–1155 (2011).

[113] Pino, J. del, Feist, J., and Garcia-Vidal, F. J., "Quantum theory of collective strong coupling of molecular vibrations with a microcavity mode", New J. Phys. **17**, 053040 (2015).

[114] Holstein, T. and Primakoff, H., "Field dependence of the intrinsic domain magnetization of a ferromagnet", Phys. Rev. **58**, 1098–1113 (1940).

[115] Bullough, R. K., "Photon, quantum and collective, effects from rydberg atoms in cavities", Hyperfine Interact. **37**, 71–108 (1987).

[116] Hopfield, J. J., "Theory of the contribution of excitons to the complex dielectric constant of crystals", Phys. Rev. **112**, 1555–1567 (1958).

[117] Deng, H., Haug, H., and Yamamoto, Y., "Exciton-polariton Bose-Einstein condensation", Rev. Mod. Phys. **82**, 1489–1537 (2010).

[118] Kockum, A. F., Miranowicz, A., Liberato, S. D., Savasta, S., and Nori, F., "Ultrastrong coupling between light and matter", Nat. Rev. Phys. **1**, 19–40 (2019).

[119] Gambino, S. et al., "Exploring light–matter interaction phenomena under ultrastrong coupling regime", ACS Photonics **1**, 1042–1048 (2014).

[120] Genco, A., Ridolfo, A., Savasta, S., Patanè, S., Gigli, G., and Mazzeo, M., "Bright polariton coumarin-based OLEDs operating in the ultrastrong coupling regime", Adv. Opt. Mater. **6**, 1800364 (2018).

[121] Eizner, E., Brodeur, J., Barachati, F., Sridharan, A., and Kéna-Cohen, S., "Organic photodiodes with an extended responsivity using ultrastrong light–matter coupling", ACS Photonics **5**, 2921–2927 (2018).

[122] George, J., Chervy, T., Shalabney, A., Devaux, E., Hiura, H., Genet, C., and Ebbesen, T. W., "Multiple Rabi splittings under ultrastrong vibrational coupling", Phys. Rev. Lett. **117**, 153601 (2016).

[123] Mueller, N. S., Okamura, Y., Vieira, B. G. M., Juergensen, S., Lange, H., Barros, E. B., Schulz, F., and Reich, S., "Deep strong light–matter coupling in plasmonic nanoparticle crystals", Nature **583**, 780–784 (2020).

[124] Michelson, A. A., "Visibility of interference-fringes in the focus of a telescope", The London, Edinburgh, and Dublin Philosophical Magazine and Journal of Science **31**, 256–259 (1891).

[125] Michelson, A. A., "XXX. On the application of interference methods to spectroscopic measurements.—II", The London, Edinburgh, and Dublin Philosophical Magazine and Journal of Science **34**, 280–299 (1892).

[126] Lord Rayleigh, "XLVII. On the interference bands of approximately homogeneous light; in a letter to Prof. A. Michelson", The London, Edinburgh, and Dublin Philosophical Magazine and Journal of Science **34**, 407–411 (1892).

[127] Fellgett, P., "Theory of infra-red sensitivities and its application to investigations of stellar radiation in the near infra-red", PhD thesis (University of Cambridge, 1949).

[128] Cooley, J. W. and Tukey, J. W., "An algorithm for the machine calculation of complex fourier series", Math. Comput. **19**, 297–297 (1965).

[129] Heideman, M. T., Johnson, D. H., and Burrus, C. S., "Gauss and the history of the fast Fourier transform", Arch. Hist. Exact Sci. **34**, 265–277 (1985).

[130] Forman, M. L., "A fast Fourier transform technique and its application to Fourier spectroscopy", Le Journal de Physique Colloques **28**, C2–58–C2–61 (1967).

[131] Griffiths, P. R. and de Haseth, J. A., *Fourier Transform Infrared Spectrometry*, 2nd ed. (John Wiley & Sons, Apr. 20, 2007), 556 pp.

[132] Kauppinen, J. and Partanen, J., *Fourier transforms in spectroscopy* (Wiley-VCH, Berlin New York, 2001) Chap. 6, pp. 77–108.

[133] Harrick, N. J., "Surface chemistry from spectral analysis of totally internally reflected radiation", J. Phys. Chem. **64**, 1110–1114 (1960).

[134] Fahrenfort, J., "Attenuated total reflection", Spectrochim. Acta **17**, 698–709 (1961).

[135] Hecht, E., *Optics, global edition* (Pearson, 2016), 728 pp.

[136] Prati, S., Joseph, E., Sciutto, G., and Mazzeo, R., "New advances in the application of FTIR microscopy and spectroscopy for the characterization of artistic materials", Acc. Chem. Res. **43**, 792–801 (2010).

[137] Skoog, D. A., Holler, F. J., and Crouch, S. R., *Principles of instrumental analysis* (Thomson Brooks/Cole, Belmont, CA, 2007).

[138] Nelu, G. and Sonia, R., *Ewing's analytical instrumentation handbook, fourth edition*, edited by Grinberg, N. and Rodriguez, S. (CRC Press, Taylor & Francis Group, Boca Raton, FL, Feb. 2019), p. 989.

[139] Swann, S., "Magnetron sputtering", Phys. Technol. **19**, 67–75 (1988).

[140] Braun, M., "Magnetron sputtering technique", in *Handbook of manufacturing engineering and technology* (Springer London, Sept. 2014), pp. 2929–2957.

[141] Larson, R. G. and Rehg, T. J., "Spin coating", in *Liquid film coating* (Springer Netherlands, 1997), pp. 709–734.

[142] Jones, L. P., "Alignment properties of liquid crystals", in *Handbook of visual display technology* (Springer Berlin Heidelberg, 2012), pp. 1387–1402.

[143] Berreman, D. W., "Solid surface shape and the alignment of an adjacent nematic liquid crystal", Phys. Rev. Lett. **28**, 1683–1686 (1972).

[144] Virtanen, P. et al., "SciPy 1.0: fundamental algorithms for scientific computing in Python", Nat. Methods **17**, 261–272 (2020).

[145] Walt, S. van der, Colbert, S. C., and Varoquaux, G., "The NumPy array: a structure for efficient numerical computation", Comput. Sci. Eng. **13**, 22–30 (2011).

[146] Hunter, J. D., "Matplotlib: a 2d graphics environment", Comput. Sci. Eng. **9**, 90–95 (2007).

[147] Eaton, J. W., Bateman, D., Hauberg, S., and Wehbring, R., *GNU Octave version 5.1.0 manual: a high-level interactive language for numerical computations* (2019).

[148] Newville, M. et al., *Lmfit/lmfit-py 1.0.1, zenodo. http://doi.org/10.5281/zenodo.3814709*, 2020.

[149] Mitsas, C. L. and Siapkas, D. I., "Generalized matrix method for analysis of coherent and incoherent reflectance and transmittance of multilayer structures with rough surfaces, interfaces, and finite substrates", Appl. Opt. **34**, 1678 (1995).

[150] Born, M. and Wolf, E., *Principles of optics: electromagnetic theory of propagation, interference and diffraction of light* (Cambridge University Press, Cambridge New York, Oct. 1999).

[151] Pettersson, L. A., Roman, L. S., and Inganäs, O., "Modeling photocurrent action spectra of photovoltaic devices based on organic thin films", J. Appl. Phys. **86**, 487–496 (1999).

[152] Kanno, H., Holmes, R. J., Sun, Y., Kena-Cohen, S., and Forrest, S. R., "White stacked electrophosphorescent organic light-emitting devices employing MoO_3 as a charge-generation layer", Adv. Mater. **18**, 339–342 (2006).

[153] Ball, J. M. et al., "Optical properties and limiting photocurrent of thin-film perovskite solar cells", Energy Environ. Sci. **8**, 602–609 (2015).

[154] Saleh, B. and Teich, M., "Electromagnetic optics", in *Fundamentals of photonics* (John Wiley & Sons, Inc., New York, 1991), pp. 157–192.

[155] L. Kronig, R. de, "On the theory of dispersion of X-rays", J. Opt. Soc. Am. **12**, 547–557 (1926).

[156] Kramers, H. A., "La diffusion de la lumiere par les atomes", in *Atti Cong. Intern. Fisica (Transactions of Volta Centenary Congress) Como*, Vol. 2 (1927), pp. 545–557.

[157] Peiponen, K.-E., Vartiainen, E. M., and Asakura, T., *Dispersion, complex analysis and optical spectroscopy*, Vol. 147 (Springer Science & Business Media, 1999).

[158] Lucarini, V., Saarinen, J. J., Peiponen, K.-E., and Vartiainen, E. M., *Kramers-Kronig relations in optical materials research: classical theory*, Vol. 110 (Springer Science & Business Media, 2005).

[159] Rakić, A. D., Djurišić, A. B., Elazar, J. M., and Majewski, M. L., "Optical properties of metallic films for vertical-cavity optoelectronic devices", Appl. Opt. **37**, 5271 (1998).

[160] Tolstoy, V. P., Chernyshova, I., and Skryshevsky, V. A., "Absorption and reflection of infrared radiation by ultrathin films", in *Handbook of infrared spectroscopy of ultrathin films* (John Wiley & Sons, 2003) Chap. 1, pp. 1–78.

[161] Oughstun, K. E. and Cartwright, N. A., "On the Lorentz-Lorenz formula and the Lorentz model of dielectric dispersion", Opt. Express **11**, 1541 (2003).

[162] Hirai, K., Hutchison, J. A., and Uji-i, H., "Recent progress of vibropolaritonic chemistry", ChemPlusChem, 10.1002/cplu.202000411 (2020).

[163] Wong, M. Y. and Zysman-Colman, E., "Purely organic thermally activated delayed fluorescence materials for organic light-emitting diodes", Adv. Mater. **29**, 1605444 (2017).

[164] Long, J. P. and Simpkins, B. S., "Coherent coupling between a molecular vibration and fabry–perot optical cavity to give hybridized states in the strong coupling limit", ACS Photonics **2**, 130–136 (2015).

[165] George, J., Shalabney, A., Hutchison, J. A., Genet, C., and Ebbesen, T. W., "Liquid-phase vibrational strong coupling", J. Phys. Chem. Lett. **6**, 1027–1031 (2015).

[166] Shalabney, A., George, J., Hutchison, J., Pupillo, G., Genet, C., and Ebbesen, T. W., "Coherent coupling of molecular resonators with a microcavity mode", Nat. Commun. **6**, 5981 (2015).

[167] Simpkins, B. S., Fears, K. P., Dressick, W. J., Spann, B. T., Dunkelberger, A. D., and Owrutsky, J. C., "Spanning strong to weak normal mode coupling between vibrational and Fabry–Pérot cavity modes through tuning of vibrational absorption strength", ACS Photonics **2**, 1460–1467 (2015).

[168] Thomas, A. et al., "Ground-state chemical reactivity under vibrational coupling to the vacuum electromagnetic field", Angew. Chem. Int. Ed. **128**, 11634–11638 (2016).

[169] Muallem, M., Palatnik, A., Nessim, G. D., and Tischler, Y. R., "Strong light-matter coupling between a molecular vibrational mode in a PMMA film and a low-loss mid-IR microcavity", Ann. Phys. **528**, 313–320 (2016).

[170] Casey, S. R. and Sparks, J. R., "Vibrational strong coupling of organometallic complexes", J. Phys. Chem. C **120**, 28138–28143 (2016).

[171] Saurabh, P. and Mukamel, S., "Two-dimensional infrared spectroscopy of vibrational polaritons of molecules in an optical cavity", J. Chem. Phys. **144**, 124115 (2016).

[172] Vergauwe, R. M. A., George, J., Chervy, T., Hutchison, J. A., Shalabney, A., Torbeev, V. Y., and Ebbesen, T. W., "Quantum strong coupling with protein vibrational modes", J. Phys. Chem. Lett. **7**, 4159–4164 (2016).

[173] Ahn, W., Vurgaftman, I., Dunkelberger, A. D., Owrutsky, J. C., and Simpkins, B. S., "Vibrational strong coupling controlled by spatial distribution of molecules within the optical cavity", ACS Photonics **5**, 158–166 (2017).

[174] Thomas, A. et al., "Tilting a ground-state reactivity landscape by vibrational strong coupling", Science **363**, 615–619 (2019).

[175] Dunkelberger, A. D., Grafton, A. B., Vurgaftman, I., Soykal, Ö. O., Reinecke, T. L., Davidson, R. B., Simpkins, B. S., and Owrutsky, J. C., "Saturable absorption in solution-phase and cavity-coupled tungsten hexacarbonyl", ACS Photonics **6**, 2719–2725 (2019).

[176] Lather, J., Bhatt, P., Thomas, A., Ebbesen, T. W., and George, J., "Cavity catalysis by cooperative vibrational strong coupling of reactant and solvent molecules", Angew. Chem. Int. Ed. **58**, 10635–10638 (2019).

[177] Vergauwe, R. M. A., Thomas, A., Nagarajan, K., Shalabney, A., George, J., Chervy, T., Seidel, M., Devaux, E., Torbeev, V., and Ebbesen, T. W., "Modification of enzyme activity by vibrational strong coupling of water", Angew. Chem. Int. Ed. **58**, 15324–15328 (2019).

[178] Menghrajani, K. S., Fernandez, H. A., Nash, G. R., and Barnes, W. L., "Hybridization of multiple vibrational modes via strong coupling using confined light fields", Adv. Opt. Mater. **7**, 1900403 (2019).

[179] Pietron, J. J., Fears, K. P., Owrutsky, J. C., and Simpkins, B. S., "Electrochemical modulation of strong vibration–cavity coupling", ACS Photonics **7**, 165–173 (2019).

[180] Menghrajani, K. S., Nash, G. R., and Barnes, W. L., "Vibrational strong coupling with surface plasmons and the presence of surface plasmon stop bands", ACS Photonics **6**, 2110–2116 (2019).

[181] Xiang, B., Ribeiro, R. F., Li, Y., Dunkelberger, A. D., Simpkins, B. B., Yuen-Zhou, J., and Xiong, W., "Manipulating optical nonlinearities of molecular polaritons by delocalization", Sci. Adv. **5**, eaax5196 (2019).

[182] Hiura, H. and Shalabney, A., "A reaction kinetic model for vacuum-field catalysis based on vibrational light-matter coupling", ChemRxiv, chemrxiv.9275777.v1 (2019).

[183] Thomas, A., Jayachandran, A., Lethuillier-Karl, L., Vergauwe, R. M., Nagarajan, K., Devaux, E., Genet, C., Moran, J., and Ebbesen, T. W., "Ground state chemistry under vibrational strong coupling: dependence of thermodynamic parameters on the Rabi splitting energy", Nanophotonics **9**, 249–255 (2020).

[184] Xiang, B., Ribeiro, R. F., Du, M., Chen, L., Yang, Z., Wang, J., Yuen-Zhou, J., and Xiong, W., "Intermolecular vibrational energy transfer enabled by microcavity strong light–matter coupling", Science **368**, 665–667 (2020).

[185] Menghrajani, K. S. and Barnes, W. L., "Strong coupling beyond the light-line", ACS Photonics, 10.1021/acsphotonics.0c00552 (2020).

[186] Takele, W. M., Wackenhut, F., Piatkowski, L., Meixner, A. J., and Waluk, J., "Multimode vibrational strong coupling of methyl salicylate to a Fabry–Pérot microcavity", J. Phys. Chem. B **124**, 5709–5716 (2020).

[187] Hirai, K., Takeda, R., Hutchison, J. A., and Uji-i, H., "Modulation of prins cyclization by vibrational strong coupling", Angew. Chem. Int. Ed. **132**, 5370–5373 (2020).

[188] Pang, Y., Thomas, A., Nagarajan, K., Vergauwe, R. M. A., Joseph, K., Patrahau, B., Wang, K., Genet, C., and Ebbesen, T. W., "On the role of symmetry in vibrational strong coupling: the case of charge-transfer complexation", Angew. Chem. Int. Ed. **132**, 10522–10526 (2020).